CHARACTERIZATION OF HIGH EFFICIENCY NEUTRON DETECTOR LINEAR ARRAYS

by

CHRISTOPHER M. HENDERSON JR.

B.S., Kansas State University, 1999

A THESIS

submitted in partial fulfillment of the requirements for the degree

MASTER OF SCIENCE

Department of Mechanical and Nuclear Engineering
College of Engineering

KANSAS STATE UNIVERSITY
Manhattan, Kansas

2009

Approved by:

Major Professor
Dr. William L. Dunn

Copyright

Abstract

Two types of high efficiency neutron detector arrays (HENDAs), a 32-channel planar device and two trenched devices, were constructed at Kansas State University (KSU) and characterized. These HENDAs are prototypes for a detector that will be developed for the Spallation Neutron Source (SNS), which is located at Oak Ridge National Laboratory (ORNL). The general design objectives of a proposal from the KSU Semiconductor Materials and Radiological Technologies (SMART) Lab to the National Science Foundation, which led to a grant that funded this research, were reached. A spatial resolution for the HENDA prototypes of approximately 120 μm was achieved. The prototypes had relatively fast response times of approximately 1.2 μs, with rise times of 300 ns for the planar device and 200 ns for the 100-μm deep trenched device. The thermal neutron counting efficiency of one of the trenched devices was measured to be about 12%. It is expected that the goal of a 50% efficient HENDA is attainable by making trenches contained within the trenched device deeper and by stacking modules in a sandwich design.

The pulse heights produced by the HENDA prototypes were approximately 0.5 volt with noise levels of 13 mvolt, resulting in a signal to noise ratio of almost 40:1. The response of HENDA, when placed in the neutron beam from the tangential beam port of the KSU TRIGA Mark II was proportional to the reactor power from 2 kW to 512 kW. At 512 kW, the neutron flux is $\varphi = 1.08\times10^{7}$ cm^{-2} s^{-1}, and therefore HENDA can operate with negligible dead time at neutron fluxes beyond 10^{7} cm^{-2} s^{-1}. From the experimental results, HENDA is a valuable linear array detector and can be applied to experiments that are designed to study material properties and structures through methods such as neutron diffraction and imaging.

Table of Contents

List of Figures

List of Tables

Acknowledgements

I would like to acknowledge the assistances of my major professor Dr. William Dunn, Dr. Douglas McGregor and Dr. Kenneth Schultis from my graduate committee, Dr. Philip Ugorowski for his help during the characterization of the HENDA prototypes, Walter McNeil and Steve Bellinger of the SMART Lab for the design and fabrication of the HENDA prototypes, Russell Taylor and the Electronic Design Lab (EDL) for software and hardware design for the HENDA system. I also gratefully acknowledge the support from the National Science Foundation through award number DMR-0412208.

Dedication

I would like to dedicate this to my family, especially my wife Keeli Henderson, my mother Christa Henderson, and my mother-in-law Gayle Willard, for helping with the preparation of my thesis and giving me support.

Chapter 1 – Introduction

Neutron detector arrays, based on perforated semiconductors, are being developed by the Kansas State University (KSU) Semiconductor Materials and Radiological Technologies (SMART) Lab. Prototypes of these linear array detectors have been characterized. A thousand-channel detector array based on these prototypes will be built for eventual use at the Spallation Neutron Source (SNS) at Oak Ridge National Laboratory (ORNL). The semiconductor based neutron detector, or high efficiency neutron detector array (HENDA), is proposed to be used for neutron diffraction or scattering experiments. This detector is being designed to examine the microscopic structure of materials using neutron beams such as from the SNS VULCAN Engineering Diffractometer (VED), the SNS High Pressure Diffractometer (HPD), and from the High Flux Isotope Reactor (HFIR) at ORNL.

1.1 High Efficiency Neutron Detector Array

Three HENDA prototypes, a planar and two trenched devices, were developed by the SMART Lab. Each prototype consisted of 32 channels and used ^{6}LiF as the neutron sensitive material and a Si pn junction as the base for the detector. The Si detector is sensitive to light, and thus it is required that a light shield be incorporated to minimize noise produced by ambient light. Each channel had a 100-μm wide p-type silicon active region with a 10-μm n-type silicon border on each side, and was 4 cm long, as shown in Fig. 1.1. The 10-μm borders serve the purpose of isolating channels from each other and thereby eliminating channel cross-talk. In the planar device, each channel was covered with a thin layer of ^{6}LiF. In the trenched devices, a 30-μm wide trench was etched into the center of each channel, the trenches were filled with ^{6}LiF, and thin caps of ^{6}LiF were coated over the top surface of each device. There were three HENDAs based on the general design described above that were tested: a planar device, a first generation trenched device with 175-μm deep trenches, and a second generation trenched device with 100-μm deep trenches. All three contained 32 channels.

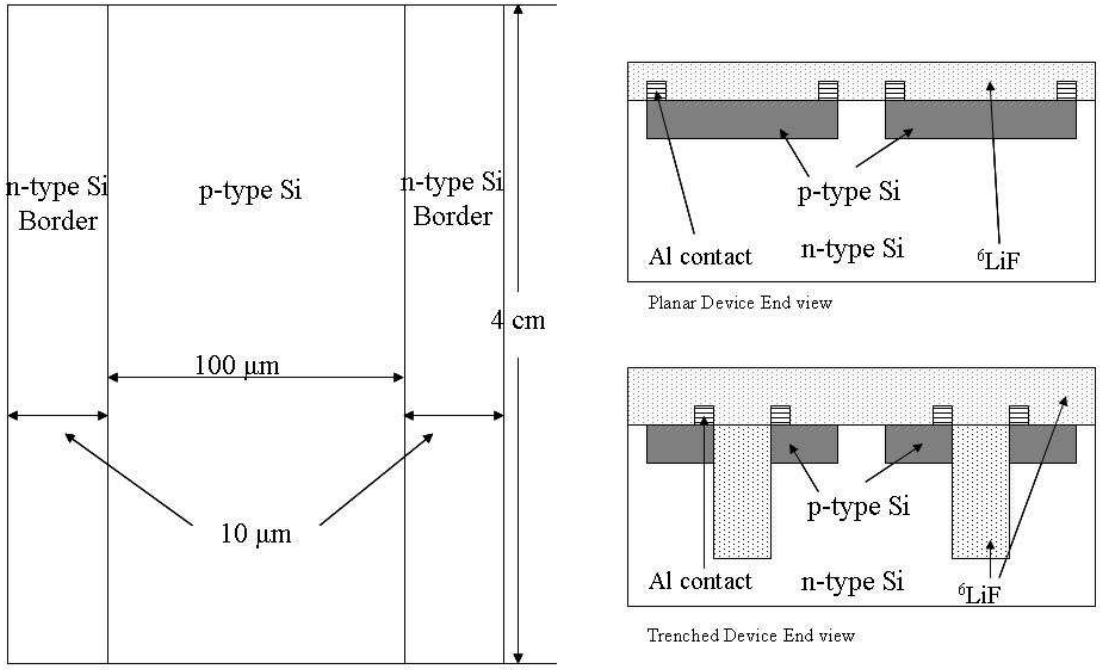

Figure 1.1. Individual HENDA channel layout (not to scale).

1.1.1 Planar Device

Each channel of the 32-channel planar device was lined along its perimeter with an aluminum contact (trace), which was then connected to a bonding pad [McNeil, et al., 2007], as shown in Fig. 1.2. Half the channels (odd channels) were connected to bonding pads at one end of the detector and the other half (even channels) to bonding pads at the other end. The aluminum trace has a lower resistance than the p-type Si material, thereby allowing the charge produced in the p-type silicon to move to the bonding pads with minimal losses. A uniform 10 μm layer of neutron sensitive ^{6}LiF was deposited over the channels.

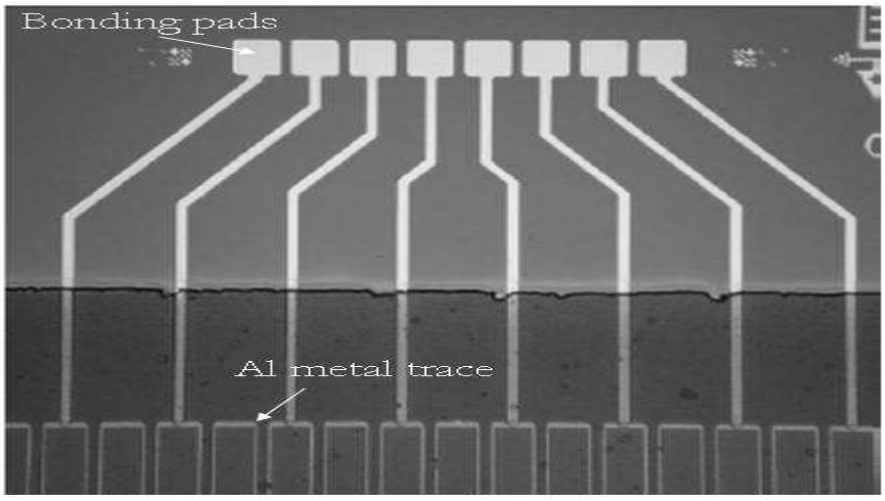

Figure 1.2. Planar device layout [McNeil, et al., 2007].

The HENDAs were mounted onto a daughter board that provides the necessary positive reverse bias voltage and sends the raw neutron pulse signal to two 16-channel PATARA I ASIC chips, which were responsible for the pre-amplification/amplification/shaping of the pulses.

1.1.2 Trenched Devices

The trenched devices used the basic design of the planar device with the exceptions that the 100 μm p-type Si material region contains a 4 cm long, 30 μm wide, straight trench through the middle of each channel, as shown in Fig. 1.3, and the individual channels were rounded and connected to larger oval bond pads. The individual trenches were backfilled with ^{6}LiF powder and capped with a uniform 26-μm layer of ^{6}LiF.

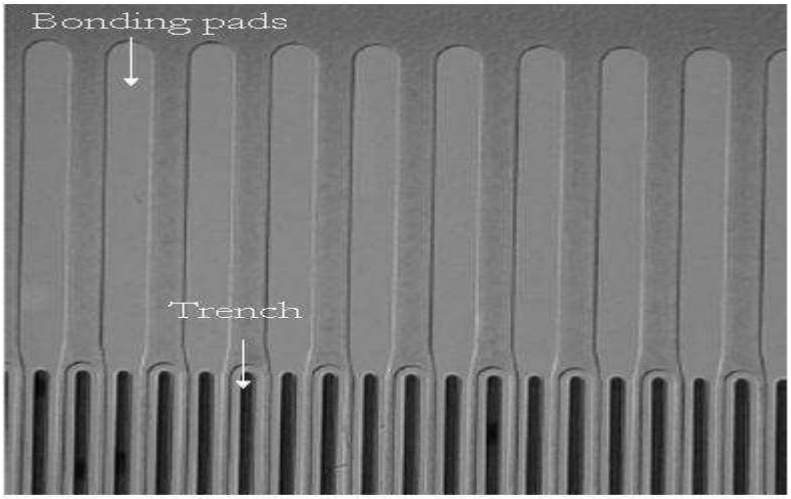

Figure 1.3. Trenched device layout [McNeil, et al., 2007].

Trenched devices with two trench depths, 175 μm and 100 μm, were constructed. In the 175-μm trenched device, the charge produced by the neutron interaction with ^{6}LiF was transported through the p-type Si material. The high resistance of Si caused losses of collected charge as the distance from the bonding pads to the neutron interaction increased. To reduce loss of collected charge, an aluminum metal trace was placed on the perimeter of each individual trench of the 100 μm deep trenched device. The aluminum traces minimized charge losses and improved charge collection within the 100-μm trenched device. Use of trenched devices with and without metal traces allowed some assessment of the effect of the aluminum traces.

1.2 HENDA Background, Design Specification, and Applications

Intense neutron sources such as the SNS and High Flux Isotope Reactor (HFIR) offer unique opportunities for material science research. In order to take advantage of these opportunities, high-resolution (sub-mm) neutron detector arrays are needed. Placing detectors near samples under investigation has the advantage of minimizing neutron interactions in air between the sample and the detector. Of the common types of neutron detectors, such as gas, scintillation, and semiconductor neutron detectors, semiconductor based neutron detectors offer the most promise for high-resolution neutron detection. The main disadvantage of semiconductor detectors is their low thermal detection efficiency of only a few percent. Given the low thermal detection efficiency they are not ideal for material science research by neutron scattering, such as neutron

diffraction. To overcome the low thermal neutron detection efficiency, a perforated semiconductor detector was developed. The perforations are filled with neutron reactive material, such as ^{6}LiF, to achieve thermal neutron detection efficiencies exceeding 10 percent [McGregor, 2007; Jahan et al, 2007; Dunn et al., 2007]. The HENDAs utilize the perforated semiconductor detector technology to achieve higher thermal neutron detection efficiency and sub-mm resolution for neutron scattering material science research.

The two principal SNS instruments that could utilize HENDAs are the VED and the HPD, which utilize neutron diffraction for material science research. Each instrument line requires thermal neutron detectors capable of spatial resolution from 100 to 500 μm, relatively fast response times (on the order of 10 μs or less), and insensitivity to gamma rays [McGregor, 2007]. The prototype HENDAs satisfied these requirements.

Other instruments involving material science research using neutron diffraction that could utilize the HENDA include the Neutron Powder Diffractometer (HB-2A) and the Neutron Residual Stress Mapping Facility (HB-2B) Instruments at the HFIR. The HB-2A instrument is used to conduct crystal structural and magnetic structural studies of powdered and ceramic samples [Chakuomakos, 2008]. The HB-2B instrument is used to scan residual stresses in engineering materials such as welds, forgings, extrusions, bearings, material under applied stresses and piezoelectric materials under the influence of electric fields [Hubbard, 2008]. The detectors in use have spatial resolutions on the order of a few millimeters. Using a HENDA at these HFIR instruments with current design specifications for resolution will help materials scientists achieve a better understanding of materials.

1.3 Research Objective

The primary objective of the research reported in this thesis was to characterize 32-channel semiconductor linear-array neutron detector prototypes designed and fabricated by the SMART Laboratory at KSU. One planar (coated) prototype with aluminum traces, one 175-μm deep trenched (filled and coated) prototype without aluminum traces, and one 100-μm deep trenched (filled and coated) prototype with aluminum traces were characterized.

Chapter 2 – Semiconductor Theory

Neutrons do not have an electric charge, and thus do not ionize directly. However, they do produce secondary particles that ionize. The most common secondary method for detecting neutrons is through charged particles that are produced in nuclear reactions. Three of the materials commonly used to detect neutrons are boron, lithium, and uranium. When neutrons interact with any of these materials in a detector, charged-particle reaction products are produced, which can be detected.

2.1 Lithium and Boron

Lithium and boron are the two materials that were considered for the neutron sensitive material to be used for the HENDA. Each material has its advantages and disadvantages for being used as the neutron sensitive material. One consideration in the decision of choosing a neutron sensitive material is the neutron absorption cross section, σ_a. The ^{6}Li and ^{10}B isotopes have larger thermal neutron cross-sections than the ^{7}Li and ^{11}B isotopes. The ^{10}B and ^{6}Li absorption cross sections are shown in Fig. 2.1 as functions of neutron energy E. At neutron energies $E \leq 0.05$ MeV, σ_a is proportional to $1/v$, where v is the velocity of a neutron of energy E.

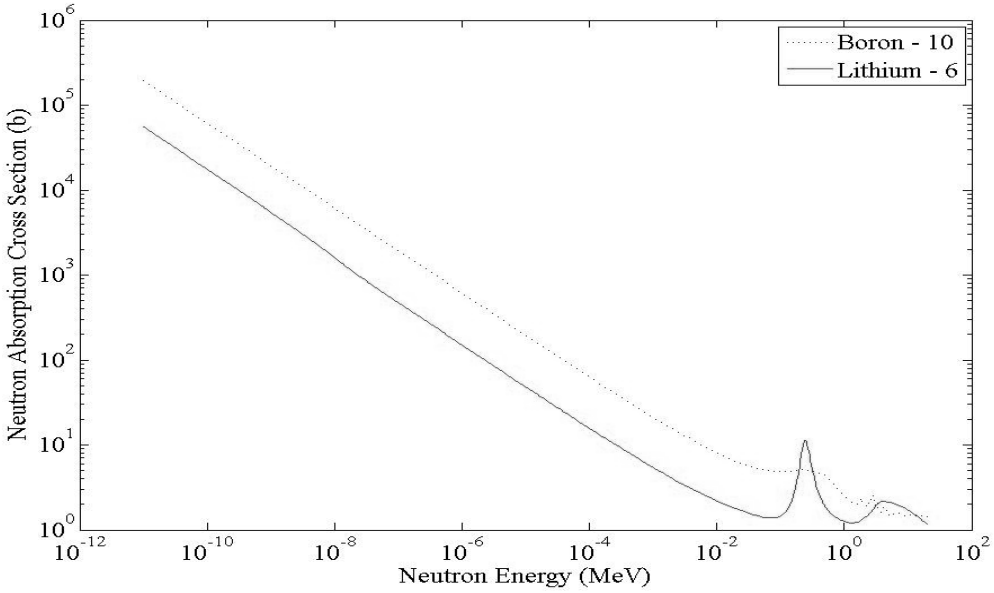

Figure 2.1. Absorption cross-section versus neutron energy for ^{6}Li and ^{10}B interactions [Brookhaven, 2006].

A second consideration when choosing a neutron sensitive material for a neutron detector is what products are produced by the neutron interaction with the material. When neutrons are absorbed by ^{6}Li, the following reaction occurs

$$^{6}_{3}\mathrm{Li} + {}^{1}_{0}\mathrm{n} \rightarrow {}^{3}_{1}\mathrm{H} + {}^{4}_{2}\mathrm{He},$$

which has a total Q-value of 4.78 MeV. The ^{3}H reaction product leaves with a kinetic energy of 2.73 MeV while the ^{4}He product has a kinetic energy of 2.05 MeV.
Two absorption reactions occur in ^{10}B. One is

$$^{10}_{5}\mathrm{B} + {}^{1}_{0}\mathrm{n} \rightarrow {}^{7}_{3}\mathrm{Li} + {}^{4}_{2}\mathrm{He}\,(\text{to ground state of } {}^{7}\mathrm{Li}),$$

which has a total Q-value of 2.79 MeV. The ^{7}Li reaction product leaves with a kinetic energy of 1.02 MeV while the ^{4}He product has a kinetic energy of 1.77 MeV. The other absorption reaction is

$$^{10}_{5}\mathrm{B} + {}^{1}_{0}\mathrm{n} \rightarrow {}^{7}_{3}\mathrm{Li} + {}^{4}_{2}\mathrm{He}\,(\text{to first excited state of } {}^{7}\mathrm{Li}),$$

which has a total Q-value of 2.31 MeV. The ^{7}Li reaction product has a kinetic energy of 0.84 MeV while the ^{4}He product has a kinetic energy of 1.47 MeV. In the ^{10}B(n, α)^{7}Li reaction, the ^{7}Li goes to the ground state only 6% of the time; the other 94% of the time, ^{7}Li remains in an excited state and produces a 480 keV gamma ray [Turner, 1995]. The total Q-value for the ^{6}Li reaction is larger than the Q-values for either ^{10}B reaction. This gives ^{6}Li a distinct advantage over ^{10}B when used for a solid-state thermal neutron detector, even with a smaller average neutron absorption cross-section, because the ranges of the reaction products from ^{6}Li are larger than those of the reaction products from ^{10}B. The large Q-value of the ^{6}Li absorption reaction helps in discrimination of neutron pulses from those of noise or gamma rays. Given the advantages and disadvantages, ^{6}LiF was chosen as the neutron sensitive material for the HENDAs and, thus, only ^{6}LiF is considered as the neutron reactive material in the reminder of this thesis.

2.2 Basic Concept of Neutron Semiconductor Detectors

Thin film semiconductor HENDAs operate on the basic concept of detecting the secondary charged particles resulting from a neutron being absorbed in the ^{6}LiF layer. The ranges and stopping powers of the charged particles play important roles in

determining the ^{6}LiF layer thickness of the detector, because a neutron can interact anywhere within the ^{6}LiF layer.

2.2.1 Heavy Charged Particle Stopping Power and Range

A charged particle of initial kinetic energy, T_o, slows to a kinetic energy $T(x)$ after traveling a distance x through a given material. In general, slowing of the charged particle is caused both by Coulombic interactions with atomic electrons and nuclei and by radiation losses (bremsstrahlung). The stopping power, $-dT/dx$, is relatively constant for heavy charged particles at high energy but, as the charged particle slows down $-dT/dx$, generally increases until the energy of the charged particle is low enough for charge neutralization or quantum effects to bring about a sharp reduction in stopping power. The average distance the charged particle travels before being stopped is called the mean range R.

For heavy charged particles, such as alpha particles and tritons that have kinetic energies much less than their rest-mass energies, slowing down is almost entirely due to Coulombic interactions. If a multitude of Coulombic interactions takes place, the slowing down is virtually continuous and essentially along a straight-line path. The interactions individually may range from ionization processes, producing energetic recoil electrons, to weak atomic or molecular excitation, which may not result in ionization at all. The stopping power that results from Coulombic interactions, $(-dT/dx)_{coll}$, is called collisional stopping power or ionization stopping power [Faw and Shultis, 1993].

The collisional stopping power of a heavy charged particle depends on its atomic number Z, the speed of the particle v, the density of the stopping medium ρ, the atomic mass A, and the effective ionization potential of the medium I [Faw and Shultis, 1993]. The ionization potential for heavy charged particles can be described by the Bragg ionization curve [McGregor, et al., 2003]

$$I(x) = \int_0^{\infty} \frac{i(r-x)}{\gamma\sqrt{\pi}} \exp[-(\frac{r-R}{\gamma})^2]dr \,, \tag{2.1}$$

where R is the mean range of the heavy charged particle, x is the distance that the heavy charged particle has traveled in the medium, i is the specific ionization, and γ is the straggling parameter. For elements of Z greater than or equal to 13, the ionization

potential in units of eV can be approximated by the following empirical formula [Faw and Shultis, 1993]

$$I = 9.76Z + 58.8Z^{-0.19}, \tag{2.2}$$

and for compounds I should be increased by a factor of 1.13 [Faw and Shultis, 1993]. For elements of $Z<13$, I is given by [Cottingham and Greenwood, 2001]

$$I = 12Z. \tag{2.3}$$

Knowing the ionization potential of the medium that the heavy charged particle is traveling through, the stopping power can be determined by the following approximation, which is valid for heavy particles having energies between 2 and 10 MeV [Faw, 1993],

$$\left(-\frac{dT}{dx}\right)_{coll} = \rho\left(\frac{Z}{A}\right)z^2\left(4\pi N_a r_e^2 m_e c^2\right)\beta^{-2}\left[\ln\left(\frac{2m_e c^2\beta^2}{(1-\beta)I}\right)-\beta^2\right], \tag{2.4}$$

where N_a is Avogadro's number, z is the charge of the heavy charged particle, r_e is the classical electron radius, Z and A are the atomic number and atomic mass of the nuclei in the medium, ρ is the density of the medium, m_e is the rest mass of the electron, and β is the ratio of the speed of the particle to the speed of light

$$\beta = \frac{v}{c} = \frac{\sqrt{T^2 + 2TMc^2}}{T + Mc^2}, \tag{2.5}$$

with M the rest mass of the heavy particle and c the speed of light. Note that to use this formula, units for $m_e c^2$ and I must be the same [Faw and Shultis, 1993].

Charged particles of initial energy T_o are characterized by a range R, although specific particles travel slightly different distances due to statistical fluctuations in the energy losses along their tracks in a given medium. The following assumption is made to calculate the range of a charged particle: neglect the energy-loss fluctuations and assume particles lose energy continuously along their tracks with a mean energy loss per unit path length determined from the total stopping power. Given these assumptions the range of a charged particle is given by [Faw and Shultis, 1993]

$$R = \int_0^{T_o} \frac{dT}{\left(dT/dx\right)_{Total}}. \tag{2.6}$$

From Figs. 2.2 and 2.3 it is evident that the triton is the particle that most often will be detected from the ^{6}Li(n,α)^{3}H reaction and the range of the triton is about 32 μm. Thus,

the ^{6}LiF cap layer should not exceed 32 μm, because no charged particles produced further than 32 μm from the diode material can be detected.

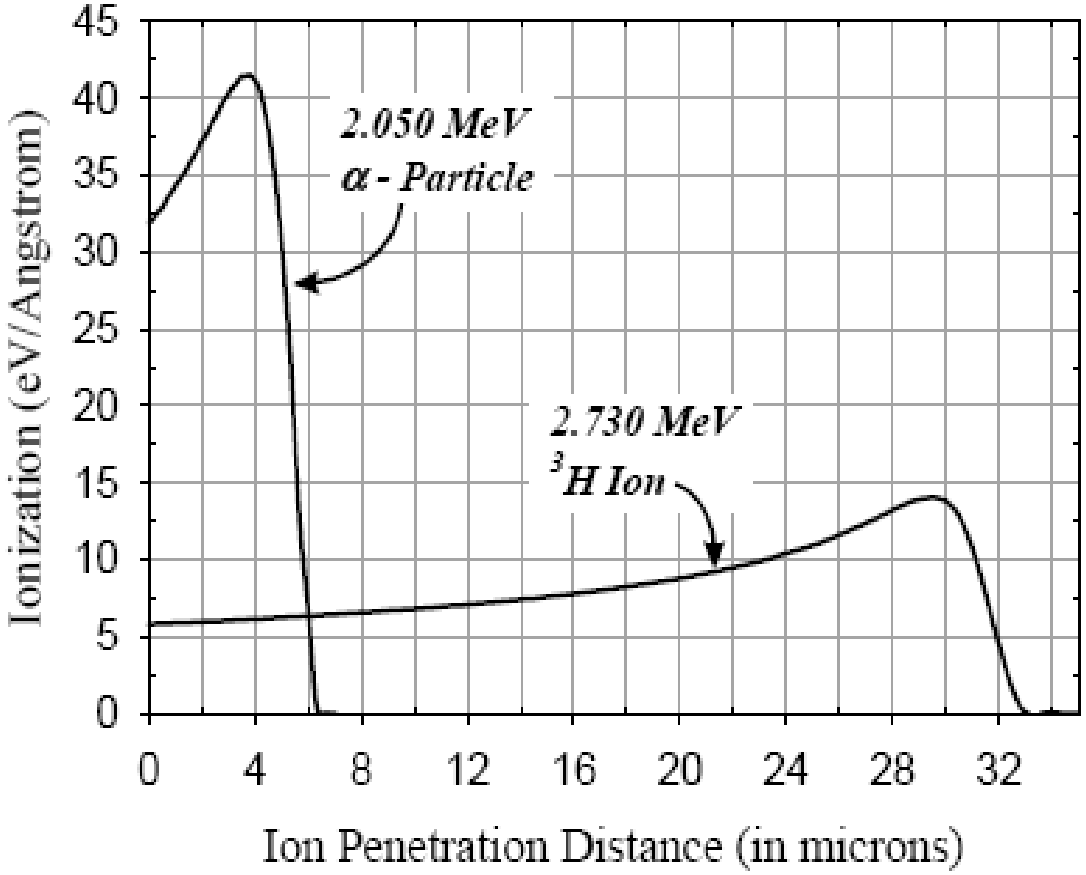

Figure 2.2. Energy loss per unit length (denoted ionization) in ^{6}LiF film as described by the Bragg distribution for the two charged particle products of the ^{6}Li(n,α)^{3}H reaction [McGregor, et al., 2003].

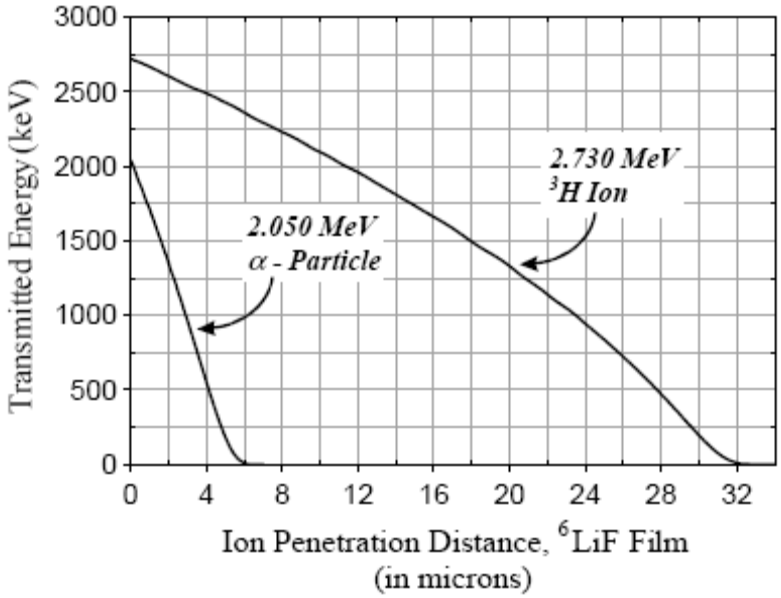

Figure 2.3. Transmitted energy remaining after the particle has traveled a penetration distance x in the film coating as a function of penetration distance. The energy deposited in the detector is the difference between the original particle energy and the transmitted energy [McGregor, et al., 2003].

2.2.2 Neutron Interaction in the Detector

When a neutron interacts with the ^{6}LiF in a trench of a HENDA, it produces charged particles that may be detected by the semiconductor layer as shown schematically in Fig. 2.4. As the neutrons are absorbed in the ^{6}LiF layer of the detector, the reaction releases charged particles in opposite directions. One or both of the charged particles may enter the semiconductor layer. When a charged particle enters the semiconductor it loses its energy through Columbic scattering. The Columbic scattering of the charged particle creates a high density plasma cloud of columnar ionization in the form of electron-hole pairs. To ensure that the electron-hole pairs are separated and move to their respective contacts, a positive reverse bias voltage is placed on the semiconductor [McGregor, et al., 2003]. The electrons move toward the +1.4 volt reverse bias voltage and the holes move toward ground. In the p-type Si material the holes are the majority carriers.

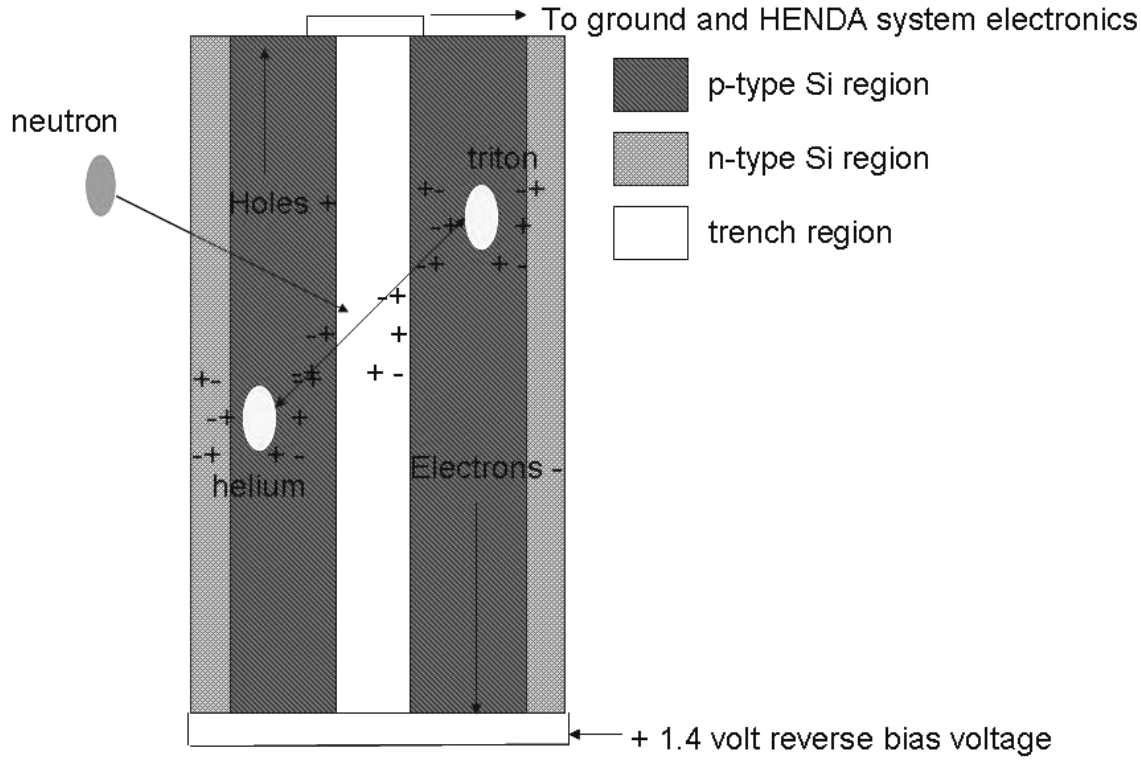

Figure 2.4. Top view of a possible neutron interaction in the ^{6}LiF-filled trench of a trenched semiconductor neutron detector, leading to two charged particles that enter the active p-type Si region.

2.3 HENDA Estimated Neutron Detection Efficiency

The HENDA efficiency is also dependent on the neutron absorption cross-section of the ^{6}Li material. As neutron energy (velocity) increases the efficiency of the detector generally decreases, because the cross-section of the neutron reactive material generally decreases with neutron energy.

2.3.1 Neutron Detection Efficiency Model Development for the Planar Device

To estimate the planar device neutron counting efficiency, the following probability density function (PDF) was used

$$f(x) = N\sigma_a \exp\left[-N\sigma_a(E)x\right], \tag{2.7}$$

where $\sigma_a(E)$ is microscopic absorption cross-section of ^{6}Li at neutron energy E, N is atomic density of ^{6}Li, and x is distance. For a cap layer of thickness d, the PDF can be

integrated to estimate the probability of a neutron interaction within the cap. For a neutron at normal incidence this probability is

$$F(d) = 1 - \exp[-N\sigma_a(E)d]. \tag{2.8}$$

Not every interaction leads to a count because the charged particles are emitted in arbitrary directions.

Given that an array of total width W is composed of n channels each with an active width w, the fraction a of the detector area that is active is given by

$$a = \frac{nw}{W}. \tag{2.9}$$

This leads to an equation for the neutron counting efficiency for the planar device of the form

$$\varepsilon_{planar}(E) = C_p(d)\{1 - \exp[-aN\sigma_a(E)d]\}, \tag{2.10}$$

where C_p will be determined by experimental methods for the specific cap thickness of the planar device [McGregor, et al., 2003].

2.3.2 Neutron Detection Efficiency Model Development for the Trenched Device

The efficiency was estimated only for the 100 μm deep trenched device. The neutron counting efficiency model for the trenched device must account for the ^{6}LiF in the trenches. A trenched device contains trenches of width w_t and trench depth D and the trenched device neutron detection efficiency is estimated to be [McGregor, et al., 2003]

$$\begin{aligned}\varepsilon_{trench}(E) = {} & C_{t_1}(d)\frac{w - w_t}{w}\{1 - \exp[-aN\sigma_a(E)d]\} \\ & + C_{t_2}(d, D)\frac{w_t}{w}\{1 - \exp[-aN\sigma_a(E)(d + D)]\}\end{aligned}. \tag{2.11}$$

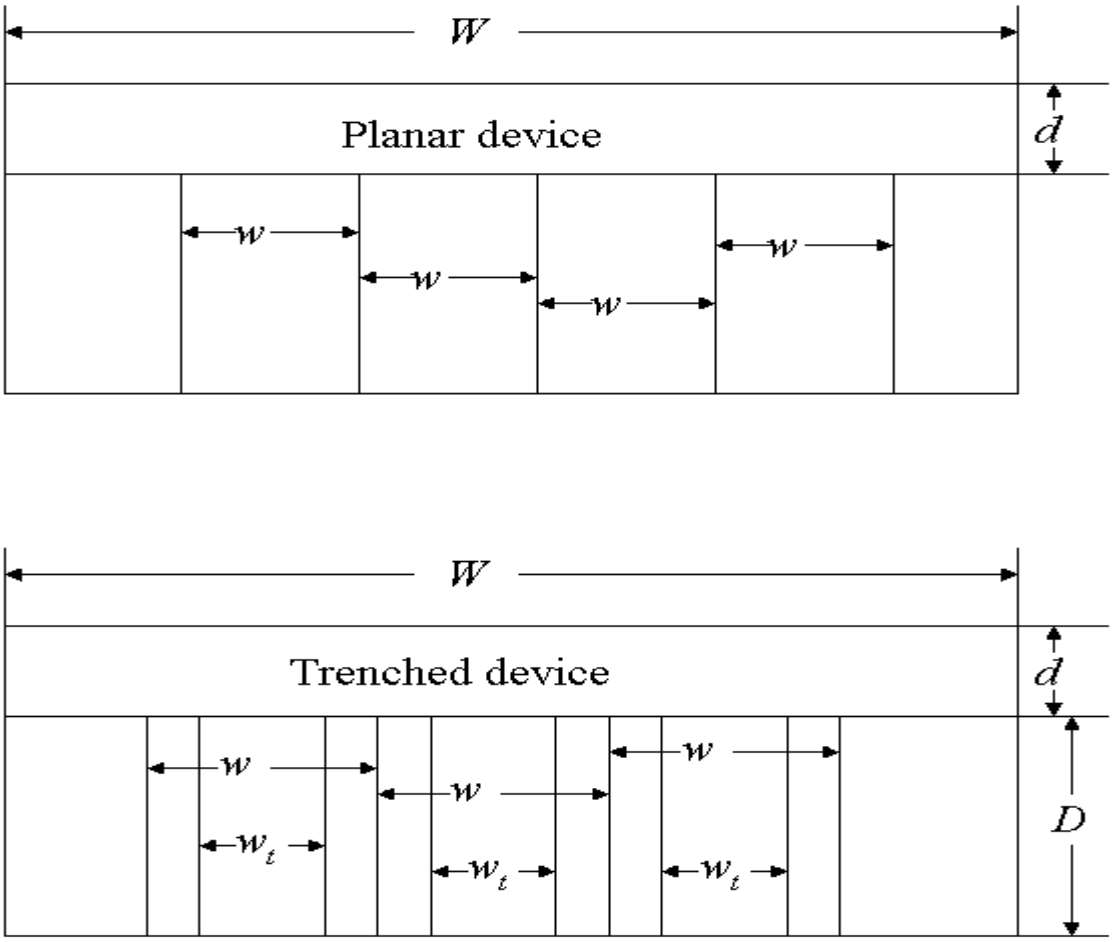

Figure 2.5. Cross-sectional view of the planar and trenched devices.

2.3.4 HENDA Estimated Neutron Counting Efficiency Model Results

With $Cp=C_{t1}=C_{t2}=1$, the models estimate the maximum possible efficiency because they do not take into account the fact that some charged particles will be emitted in directions that preclude them from reaching the diode material. The parameters that were used to determine the estimated neutron detection efficiencies for the planar and trenched devices are given in Table 2.1.

Table 2.1 Neutron detection efficiency model parameters

Device	*D* (μm)	*w* (μm)	*W* (cm)	w_t (μm)	*D* (μm)
Planar	10	120	0.6	-	-
Trenched	26	120	0.6	30	100

Applying the absorption cross-section from Fig. 2.1 and evaluating Eqs. (2.10) and (2.11) the estimated maximum neutron counting efficiencies for the planar and 100-μm trenched devices are shown in Fig. 2.6. It can be seen that the neutron detection efficiency for the each device is approximately *1/v* for neutron energies $E \leq 0.05$ MeV.

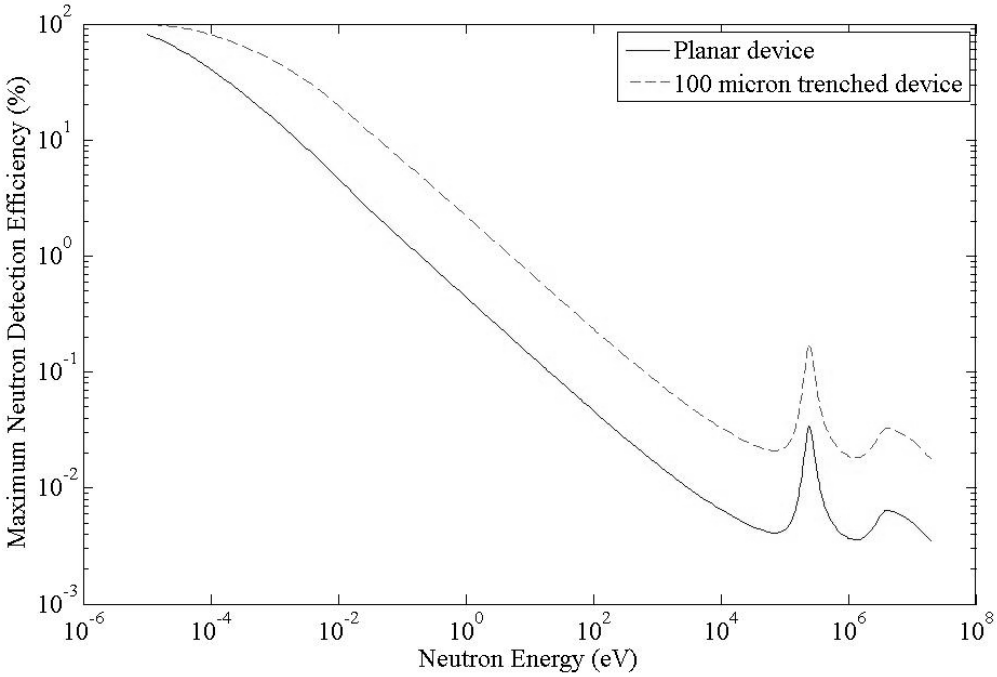

Figure 2.6. Planar and 100-μm trenched devices maximum estimated neutron detection efficiency model results from Eq. (2.10) and Eq. (2.11).

The higher efficiency of the trenched device is due to both the trenches and the thicker ^{6}LiF cap layer. The neutron detection efficiency will increase with increasing cap layer thickness until a saturation thickness is reached after which it eventually decreases (see Fig. 2.7). The saturation thickness for the planar devices is about 26 μm. Thus the ^{6}LiF cap layer should not be greater than 26 μm. Similarly, the counting efficiency will increase with trench depth, as shown in Fig. 2.8, until either structural limitations on trench depth are reached or attenuation of the neutron flux becomes appreciable. The width of the trench should not much exceed the range of a triton in ^{6}LiF, in order to increase the likelihood that a charged particle does reach the p-type silicon where the charge is collected.

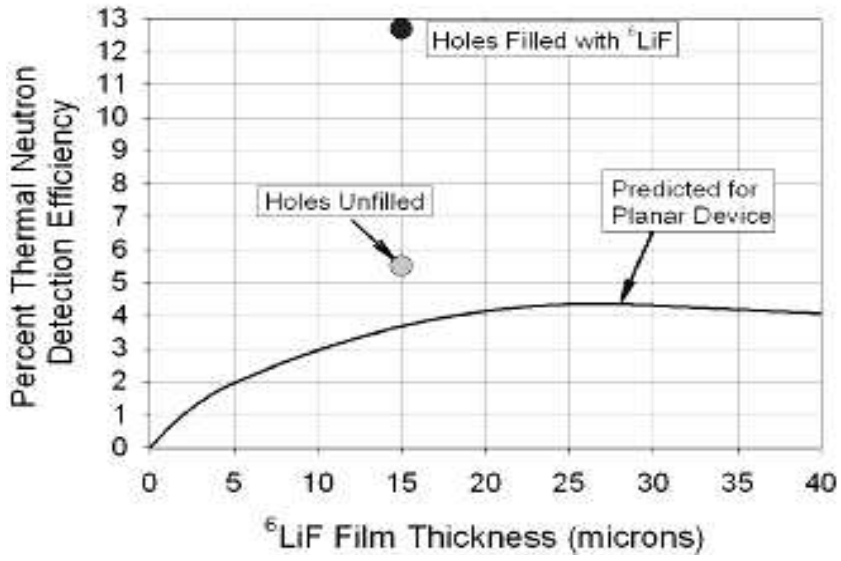

Figure 2.7. Thermal neutron detection efficiency as a function of surface ^{6}LiF film thickness, taken from [McGregor, 2007].

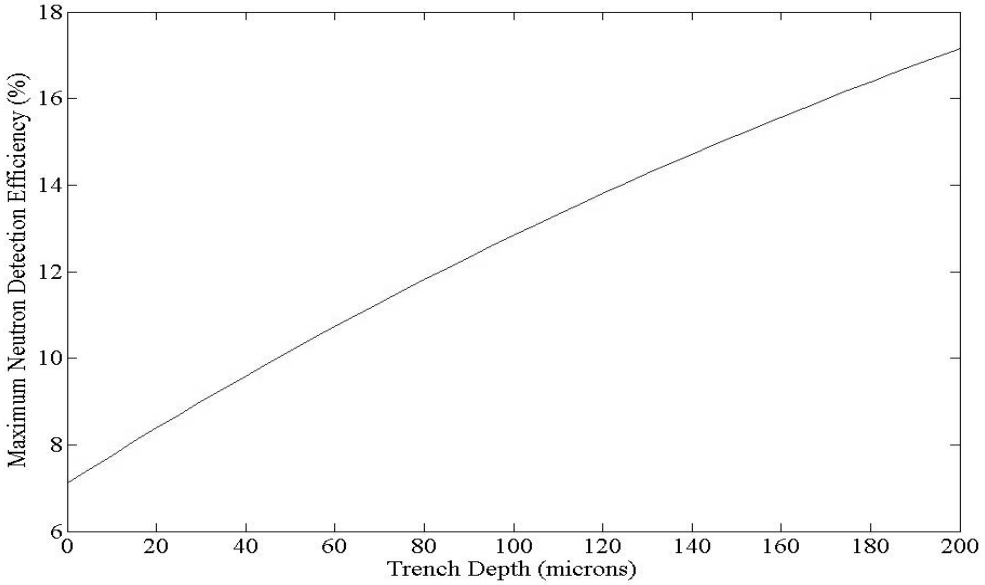

Figure 2.8. Maximum neutron detection efficiency for thermal neutron (0.0253 eV) with varying trench depth *D* using the trenched device neutron detection efficiency model Eq. (2.11).

Chapter 3 – HENDA System Operation

The HENDA system is depicted in Fig. 3.1. The detector motherboard holds two PATARA I ASIC chips (one for each end of the HENDA), which are connected to a daughter board to which the HENDA is attached. Each PATARA I chip contains 16 channels, which pre-amplify, amplify, and pulse shape the incoming signal from the HENDA [Britton, et al., 2006]. The motherboard also is connected to a micro-computer, which contains an Optical Communication Card (OCC) and digital communication server software (Dcomserver) version 2.3.2. The motherboard receives power from a power supply unit.

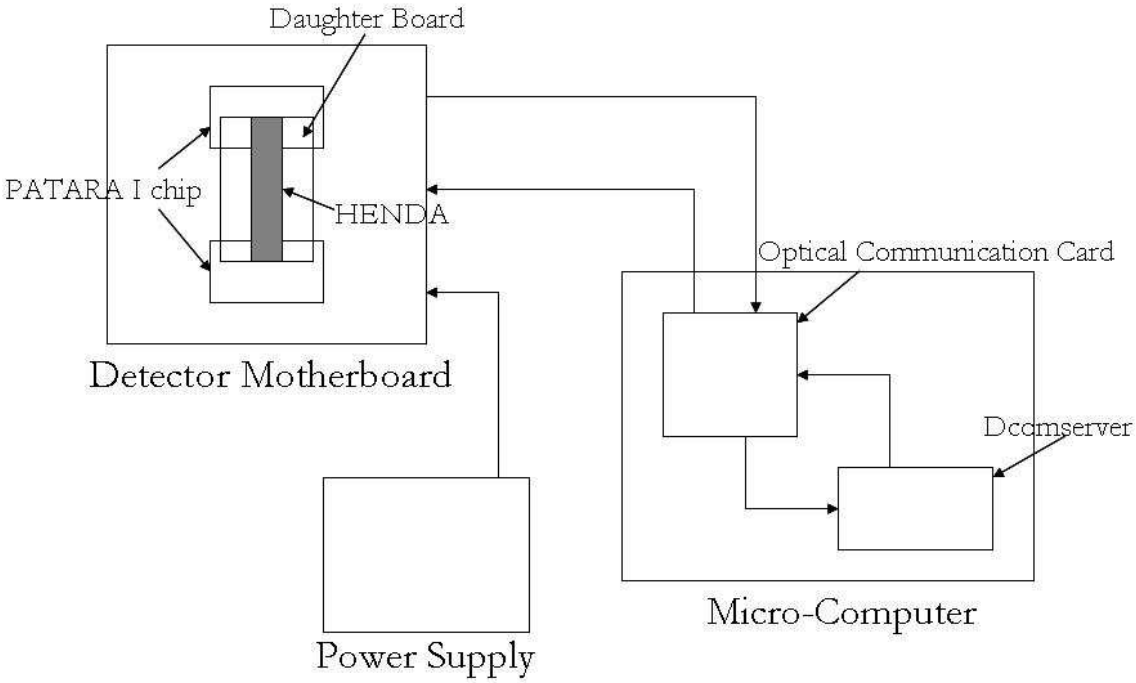

Figure 3.1. HENDA system block diagram.

3.1 Detector Motherboard

The two main functions of the detector motherboard are to provide power to each of the components contained within the detector motherboard and to transmit data collected by HENDA to the micro-computer. In addition, the detector motherboard can receive commands from the micro-computer, such as global low-level discriminator settings and start/stop acquisition.

The power supply voltages were +4.00, +6.00, and -6.00 volts. The three power supply voltages provided all the necessary power required for the components, as shown in Table 3.1. The power supply system was designed by KSU Electronic Design Lab (EDL) to minimize noise from the voltage power supply system. 24 gauge twisted tie pair wires were used to connect the three-voltage output power supply to the detector motherboard, as shown in Fig. 3.2. The 24 gauge twisted tie pair wires were chosen to minimize the electromagnetic field (EMF) noise that could interfere with detector motherboard digital communications. The transmission of data to and from the detector motherboard occurs through a pair of ethernet cables, one for transmitting data to the micro-computer and the second for receiving commands from the micro-computer.

Table 3.1. Voltage power supply and corresponding components

Voltage Power Supply (volts)	Detector System Components
+4.00	Detector motherboard digital communication
+6.00	PATARA I Chips Detector Array (+1.4 volts reverse biased voltage) Positive LLD reference voltage
-6.00	Negative LLD reference voltage

Figure 3.2. Front view of the detector motherboard showing a planar device without electromagnetic field/light shield.

3.1.1 HENDA and Daughter Board

Each HENDA was manufactured by the KSU SMART lab. Each was wire bonded by the KSU EDL to a daughter board. The daughter board contains the required components to connect the HENDA to the PATARA I chips and provides the necessary positive reverse bias voltage needed to operate a HENDA. The positive 1.4 volt reverse bias voltage is applied uniformly around the gold ring contained on the daughter board, as shown in Fig. 3.2. The wire bonds were divided into odd and even channels, with 16 channels having bonding pads at one end and the other channels having bonding pads at the other end, as shown in Fig. 1.3. Every other channel of the first generation devices are connected to a bonding pad on the top, with bonding pads for the other channels at the bottom of the HENDA [McNeil, et al., 2007]. The bonding of the detector to the daughter board allowed the detector to send its signals to one of two 16-channel PATARA I chips on the motherboard. The positive reversed bias voltage and detector signal then were transmitted through the female electric footpads, which were located at each end of the daughter board that plugged into the motherboard directly above the PATARA I chips located on each end, as shown in Fig. 3.3. A major concern was to minimize electronic noise from EMF sources and noise produced by the interaction of light with the Si detector. An aluminum shield was designed to surround HENDA, as shown in Fig. 3.4, to minimize EMF and light noise. The shield was grounded by placing a wire contact, as shown in Fig. 3.4, on the outer Al shield and attaching it to the daughter chip.

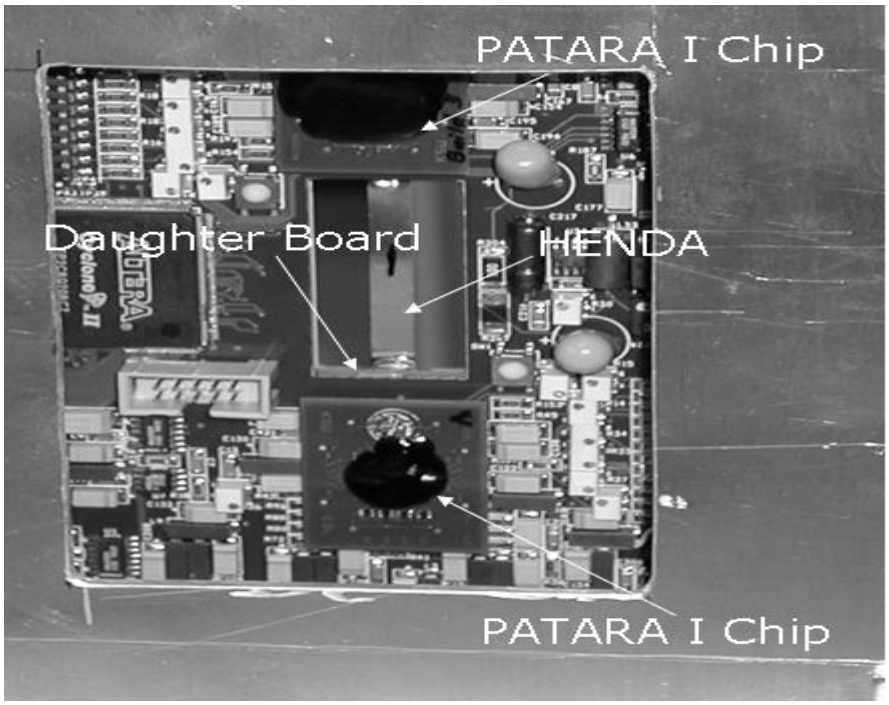

Figure 3.3. Back view of the detector motherboard showing the PATARA I chips.

Figure 3.4. HENDA within the Al EMF/light shield.

3.1.2 PATARA I ASIC Chip

The PATARA I chips were located on the backside of the detector motherboard directly behind the detector array, as shown in Fig. 3.3. Each PATARA I chip contains 16 channels, which pre-amplify, amplify, and pulse shape the incoming signal from the HENDA. The PATARA I chips featured a regulated cascade preamplifier with

adjustable gain, digitally adjustable leakage current compensation, an active feedback reset network with matching pole/zero cancellation, and input pulse polarity adjustment. The PATARA I shaper has a semi-Gaussian response, which utilizes two pairs of current-input complex-conjugate poles with gated baseline restoration [Britton, et al., 2006]. Each PATARA I dissipates a total of 59.2 mW (3.7 mW/channel) with an overall gain of 9.7 mV fC^{-1}. At full-width at half maximum (FWHM) of 5.65 mV fC^{-1} the pulse duration was 270 ns [Britton, et al., 2006].

As shown in Fig. 3.3, the distance from the PATARA I chips' bonding pads to the HENDA's bonding pads was short, approximately 1 inch. The short distance minimized signal loss from the HENDA to the PATARA I chips and minimized the noise entering the system.

3.1.3 Low Level Discriminator (LLD)

At the output of each PATARA I chip channel there was a comparator circuit that was used for the LLDs, as shown in Fig. 3.5. The input voltage V_{in} is compared to the adjustable reference voltage V_{ref}. When $V_{in} > V_{ref}$ the circuit allows the current to pass through and produces an output voltage V_{out} and is counted. If $V_{in} < V_{ref}$, then the current is not allowed to pass and no V_{out} is produced; thus no pulse is counted, minimizing pulses generated by noise from being counted.

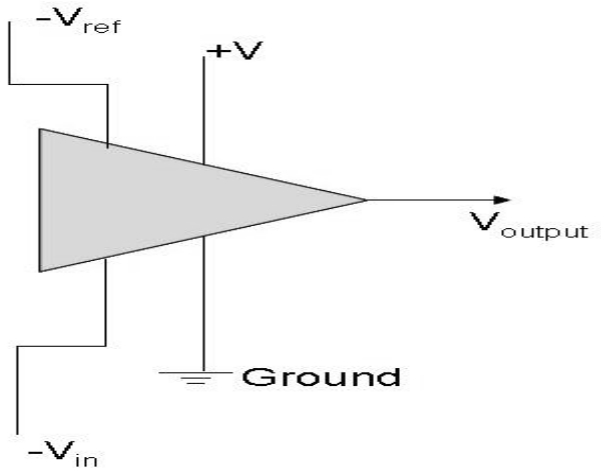

Figure 3.5. Basic comparator circuit diagram.

3.2 Optical Communication Card

Oak Ridge National Libratory (ORNL) developed the optical communication card (OCC) shown in Fig. 3.6. The OCC is contained within the micro-computer, as shown in Fig. 3.1, and is the main interface between the detector motherboard and the micro-computer. The OCC transmits the commands, such as LLD settings, from the micro-computer and receives the raw neutron interaction data from the detector motherboard, which are transmitted to the micro-computer for display.

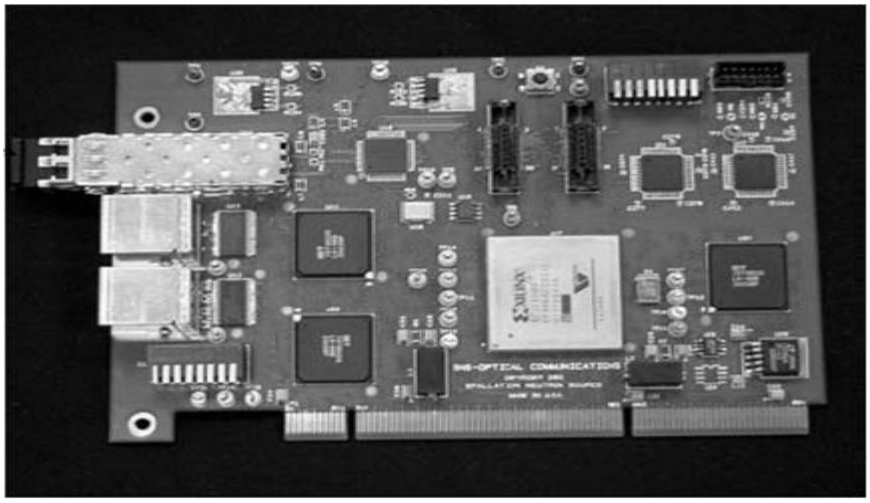

Figure 3.6. Optical Communication Card (OCC) [SNS, 2004].

3.3 Digital Communication Server Software (Dcomserver)

The Dcomserver was developed by ORNL and modified by EDL for testing and characterization of the HENDA. The software has two display screens, as shown in Fig. 3.7. The upper right hand corner display allows the user to start and stop acquisition and enter acquisition time length in seconds. It also displays elapsed time in seconds, total counts, and data acquisition system (DAS) messages. The DAS messages consist of verification of detector motherboard settings, date/time stamp for start and stop of acquisition, and display initial hardware configuration and any error that has occurred within the system.

Figure 3.7. Dcomserver version 2.3.2 displays and controls.

The main display screen displays the data in the form of histograms for each HENDA channel in a 1 second snapshot and in a cumulative snapshot. The odd and even global LLD settings can be adjusted and the user can reset for the cumulative snapshot. In addition, the users can save and load HENDA LLD settings.

The histogram data are saved in a text file and can be exported to Microsoft Excel or viewed by notepad. The file displays the date/time stamp at the beginning of the file using the start acquisition date/time stamp. Then raw neutron data are saved every second for each channel. Each 1 second of data has its time stamp. When acquisition is stopped the last row has the time data acquisition was stopped and the total counts for each channel.

Chapter 4 – Neutron Flux Measurement

Before HENDA characterization could be accomplished, the neutron flux of the neutron source had to be determined because the HENDA dead time and efficiency depends on the neutron flux. Neutron flux measurements were conducted at the KSU TRIGA mark II reactor's tangential beam port.

4.1 Gold Foil Activation Neutron Flux Measurement

Gold foil activation is a widely used method for measuring the thermal neutron flux for the following reasons: 1) naturally occurring gold is 100% ^{197}Au which has a reasonable cross-section (98.8 b) for production of ^{198}Au; 2) the metallurgy of gold is well known and chemically stable; 3) the neutron activation product ^{198}Au decays to the ground state of ^{198}Hg generally accompanied by production of a 411-keV gamma ray; 4) gold is an almost perfect 1/*v* absorber in the thermal region below about 0.2 eV; and 5) ^{198}Au has a half life of about 2.7-days, which makes it relatively easy to produce and to count. The decay scheme for ^{198}Au is not complex and for 98.68% of the disintegrations that occur a beta particle is emitted (the maximum beta energy is 961 keV), followed by emission of a 411 keV gamma ray with an emission yield of 95.51%, as shown in Fig. 4.1. Sufficient activation of ^{198}Au can be achieved in reasonable irradiation times (minutes to hours, depending on the flux) because of the absorption cross-section of ^{197}Au and the half-life of ^{198}Au. If the gold foil is too radioactive, it can be allowed to decay before counting, and can be reused in about a month's time with no appreciable activity present.

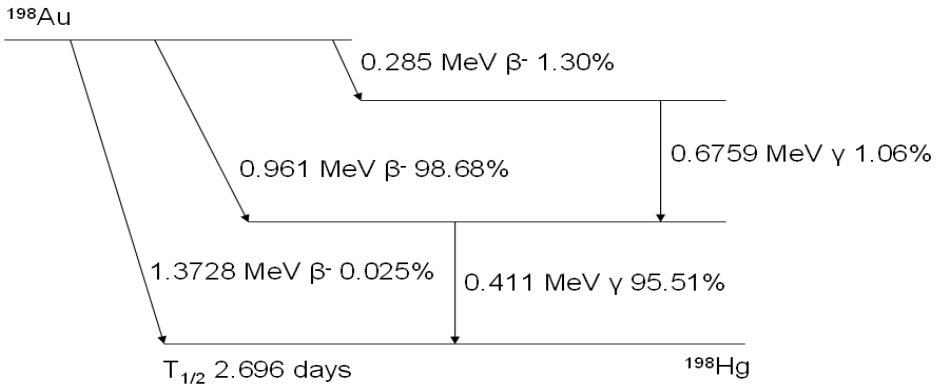

Figure 4.1. ^{198}Au decay scheme [Faw, 1993].

4.1.1 Gold Foil Activation Theory

The measurement of the neutron flux was conducted by measuring the gold foil activation of bare and cadmium covered gold foils. The bare gold foil activation rate R_b depends on the total neutron flux and the cadmium covered gold foil activation rate R_c depends primarily on the fast neutron flux. One can estimate the thermal and epithermal flux densities from these two activation rates.

If the neutron flux $\varphi(E)$ is constant throughout the volume of the bare gold foil, then the rate at which ^{198}Au is produced by ^{197}Au absorbing neutrons is

$$R_b = \frac{N_a m_b}{A} \int_0^\infty \sigma_a(E)\varphi(E)dE \,, \tag{4.1}$$

where N_a is Avogadro's number, A is the atomic mass of ^{197}Au, m_b is the mass of the gold foil, $\sigma_a(E)$ is the microscopic absorption cross-section of ^{197}Au, E is the neutron energy, and $\varphi(E)$ is the energy-dependent neutron flux [Shultis, 2002]. The neutron flux is separated into two components: the thermal neutron flux given by

$$\varphi_t = \int_0^{E_{TC}} \varphi(E)dE \tag{4.2}$$

and the fast neutron flux φ_f is given by

$$\varphi_f = \int_{E_{TC}}^{E_{\max}} \varphi(E)dE \,, \tag{4.3}$$

where E_{max} (often taken to be 10 MeV) is the effective maximum neutron energy and E_{TC} = 0.2 eV is the thermal neutron cutoff energy.

For the ease of solving Eqs. (4.2) and (4.3) some approximation must be made with respect to the neutron flux. If $E < E_{TC}$ then the neutron flux spectrum can be approximated by the Maxwellian distribution

$$\varphi(E) = \varphi_M(E) = \varphi_t \frac{E}{E_T^2} \exp\left(-\frac{E}{E_T}\right), \tag{4.4a}$$

where E_T is the most probable neutron energy for the thermal neutron flux (0.0253 eV for a temperature of T = 293 K), and the thermal neutron flux φ_T is given by [Duderstadt and Hamilton, 1976]

$$\varphi_t = 2n_o\left(\frac{1.28\times10^4\sqrt{T}}{\pi}\right)^{1/2}, \tag{4.4b}$$

where n_o is the neutron number density in the medium. If $E > E_{TC}$ the neutron can be approximated as

$$\varphi(E) = \frac{\varphi_o}{E}, \tag{4.5}$$

where φ_o is a fast neutron flux constant. The activation rate of bare gold foil thus can be written as

$$R_b = \frac{N_a m_b}{A}\left[\int_0^{E_{TC}} \sigma_a(E)\varphi_M(E)dE + \int_{E_{TC}}^{E_{\max}} \frac{\varphi_o\sigma_a(E)}{E}dE\right]. \tag{4.6}$$

For neutron energies below E_{TC} gold is assumed to be a 1/*v* absorber and thus

$$\sigma_a(E) = \sigma_{a0}\sqrt{\frac{E_o}{E}}, \tag{4.7}$$

where σ_{a0} is the gold absorption cross-section at the thermal reference energy $E_o = E_{T=293K}$ = 0.0253 eV. Thus Eq. (4.6) can be written as

$$R_b = \frac{N_a m_b}{A}\left\{\int_0^{E_{TC}} \sigma_{a0}\sqrt{\frac{E_0}{E}}\varphi_M dE + \int_{E_{TC}}^{E_{\max}} \frac{\varphi_o\sigma_a(E)}{E}dE\right\}. \tag{4.8a}$$

But by definition, the average thermal absorption cross section is given by

$$\overline{\sigma}_a = \frac{\int_0^{\infty} \sigma_a(E)\sqrt{\frac{E_o}{E}}\varphi_M(E)dE}{\varphi_t} \tag{4.8b}$$

and thus Eq. (4.8) can be written as

$$R_b = \frac{N_a m_b}{A}\left[\overline{\sigma}_a\varphi_t + \int_{E_{TC}}^{E_{\max}} \frac{\varphi_0\sigma_a(E)}{E}dE\right] \tag{4.8c}$$

The cadmium cutoff neutron energy is usually taken to be E_{CC} = 0.4 eV, and thus Eq. (4.8c) can be written as

$$R_b = \frac{N_a m_b}{A}\left[\overline{\sigma}_a + \varphi_o\int_{E_{TC}}^{E_{CC}} \frac{\sigma_a(E)}{E}dE + \varphi_o\int_{E_{CC}}^{E_{\max}} \frac{\sigma_a(E)}{E}dE\right]. \tag{4.8d}$$

The absorption cross section is still considered to be given by Eq. (4.7) up to E_{CC}. Substituting Eq. (4.7) into Eq. (4.8d) and evaluating the integral between E_{TC} and E_{CC}, R_b can be written as [Lamarsh, 2002]

$$R_b = \frac{N_a m_b}{A}\left[\bar{\sigma}_a\varphi_t + \bar{\sigma}_a\varphi_0\sqrt{\frac{16E_T}{\pi}}\left(\frac{1}{\sqrt{E_{TC}}} - \frac{1}{\sqrt{E_{CC}}}\right) + \varphi_o\int_{E_{CC}}^{E_{\max}}\frac{\sigma_a(E)}{E}dE\right]. \tag{4.9}$$

The final approximation that is made is for the third integral. Above E_{CC} gold's absorption cross-section has a large cross-section resonance. The remaining integral in Eq. (4.9) is called the resonance integral I_r. The resonance integral for gold has been determined by Argonne National Laboratory and is 1558 b [ANL, 1963]. Applying the final approximation and solving the third integral R_b is

$$R_b = \frac{N_a m_b}{A}\left[\bar{\sigma}_a\varphi_t + \bar{\sigma}_a\varphi_0\sqrt{\frac{16E_T}{\pi}}\left(\frac{1}{\sqrt{E_{TC}}} - \frac{1}{\sqrt{E_{CC}}}\right) + \varphi_0 I_r\right]. \tag{4.10}$$

In order to measure the thermal neutron flux, φ_t, the activation of ^{197}Au to ^{198}Au from thermal and fast neutrons must be differentiated. The method used to differentiate the activation of ^{197}Au is by using two gold foils in the experiment. One gold foil is bare and the other gold foil is covered by cadmium (Cd) cover. The Cd cover has sufficient thickness to prevent most thermal neutron from activating ^{197}Au. The activation of the ^{197}Au in the Cd cover is accomplished by neutrons from E_{CC} to E_{max} giving the following equation for the activation rate of Cd-covered gold foil

$$R_c = \frac{N_a m_c}{A}\varphi_o\int_{E_{cc}}^{E_{\max}}\sigma_a(E)\frac{dE}{E} = \frac{N_a m_c}{A}\varphi_o I_r\,. \tag{4.11}$$

The next step is to form the specific activation rates defined as $\hat{R}_b = R_b / m_b$ and $\hat{R}_c = R_c / m_c$. It is easy to see then that

$$\hat{R}_b - \hat{R}_c = \frac{N_a\bar{\sigma}_a}{A}\left[\varphi_t + \varphi_0\sqrt{\frac{16E_T}{\pi}}\left(\frac{1}{\sqrt{E_{TC}}} - \frac{1}{\sqrt{E_{CC}}}\right)\right]. \tag{4.12}$$

Substituting Eq. (4.5) into Eq. (4.3) and evaluating, the fast neutron flux is given by

$$\varphi_f = \varphi_o \ln\left(\frac{E_{\max}}{E_{TC}}\right). \tag{4.13}$$

The fast neutron flux constant can be estimated from Eq. (4.11), which gives

$$\varphi_o = \frac{\hat{R}_c A}{N_a I_r}. \tag{4.14}$$

The thermal neutron flux is sometimes approximated from Eq. (4.12) by assuming the term involving the fast flux is negligible, leading to

$$\varphi_t \cong \frac{A\left(\hat{R}_b - \hat{R}_c\right)}{N_a \bar{\sigma}_a}. \tag{4.15}$$

At other times, the cadmium ratio is used to obtain a second equation in the two unknowns φ_t and φ_0. Alternatively, the approach used here is to substitute Eq. (4.14) into Eq. (4.12) and solve for φ_t, obtaining

$$\varphi_t = \frac{A(\hat{R}_b - \hat{R}_c)}{N_a \bar{\sigma}_a} - \frac{\hat{R}_c A}{N_a I_r}\sqrt{\frac{16E_T}{\pi}}\left[\frac{1}{\sqrt{E_{TC}}} - \frac{1}{\sqrt{E_{CC}}}\right]. \tag{4.16}$$

4.1.2 Neutron Flux Measurement Correction Factors

The above equations neglect minor effects that require correction for proper neutron flux measurement [Shultis, 2002]: (1) Gold is not exactly a *1/v* absorber at the high end of the Maxwellian spectrum. (2) Some neutrons with $E < E_{CC}$ pass through the cadmium cover and activate the covered gold foil. (3) The cadmium cover also stops some neutrons with $E > E_{CC}$, so fewer fast neutrons activate a covered gold foil compared to a bare foil. (4) If the detector foil measured the neutron flux in a medium through which neutrons are diffusing, the presence of the foil with its relatively high absorption cross-section causes the neutron flux around the foil to be depressed. If neutrons are streaming through a void or air it can be assumed no neutron flux depression has occurred. (5) For neutron energies for which the gold foil has a large absorption cross-section, the outer layer of the foil shields the inner foil volume, i.e., the activation per unit volume is not uniform throughout the foil. This is particularly important for the fast neutron activation of gold foils.

4.1.2.1 Non-1/v Absorption Correction

Correcting for the non-1/v absorption of gold foils, the Wescott non-1/v correction $g_a(E_T)$ was used to correct the average thermal neutron absorption cross-

section. For a perfect *1/v* absorbing material $g_a(E_T)$ =1, and for gold at room temperature $g_a(E_T)$ = 1.005 [Shultis, 2002]. Applying the Wescott correction to the average thermal neutron cross-section Eq (4.10) can be rewritten as [Lamarsh, 2002]

$$\overline{\sigma}_a = \frac{\sqrt{\pi}}{2} g_a(E_T) \sqrt{\frac{E_o}{E_T}} \sigma_a(E_o) . \tag{4.17}$$

4.1.2.2 Cadmium Filter Correction

In an ideal high-pass neutron filter all neutrons below a sharp cutoff neutron energy would be absorbed. For neutron energies above the cutoff, the filter would be transparent. Cadmium covers of thickness 0.05 to 0.1 cm come close to the ideal high-pass neutron filter, absorbing almost all neutrons below 0.4 eV and very few above 0.6 eV [Shultis, 2002]. The cadmium filter correction factor F_{Cd} differs for an isotropic neutron flux and a perpendicular neutron beam.

If Cd-covers of thickness 0.0508 cm or thicker are used, negligible thermal neutrons reach the gold foil, but they also absorb some epithermal neutrons. The correction for the absorption of epithermal neutrons is defined as

$$F_{Cd} = \frac{\hat{R}_{epi}}{\hat{R}_c}, \tag{4.18}$$

where $\hat{R}_{epi}$ is specific activation rate in bare gold foil by epithermal neutrons. Most of the epithermal neutron activation of a gold foil is caused by the gold resonance at E_r = 4.91 eV [Shultis, 2002]. Let α represent the probability that a 4.91 eV neutron passes through a cadmium cover of thickness t_c, then R_c can be written as

$$\hat{R}_c = \alpha \hat{R}_{epi} . \tag{4.19}$$

Substituting Eq. (4.19) into Eq. (4.18) F_{Cd} then can be written as

$$F_{Cd} = \frac{1}{\alpha} . \tag{4.20}$$

The probability α that a 4.91 eV neutron interacts with cadmium covered foil depends on the incident beam of neutrons. For a perpendicular beam of neutrons, such as is emitted from the tangential beam port, α is given by

$$\alpha = \exp\left[-\Sigma_{Cd}(E_r) t_c\right], \tag{4.21}$$

and for an isotropic beam of neutrons

$$\alpha = 2E_3(\tau_c), \tag{4.22}$$

where $E_3(x)$ is the exponential integral function of order 3 and τ_c is given by

$$\tau_c = \Sigma_{Cd}(E_r)t_c, \tag{4.23}$$

with $\Sigma_{Cd}(E_r)$=0.328 cm^{-1} [Shultis, 2002]. As shown in Fig. 4.2 for Cd-covers less than 0.0508 cm, a Cd-covered correction factor is less than 1.01. However, if cadmium covered correction factor is required then

$$\hat{R}_{epi} = F_{Cd}\hat{R}_c \tag{4.24}$$

is substituted for $\hat{R}_c$ in Eqs. (4.14) and (4.16).

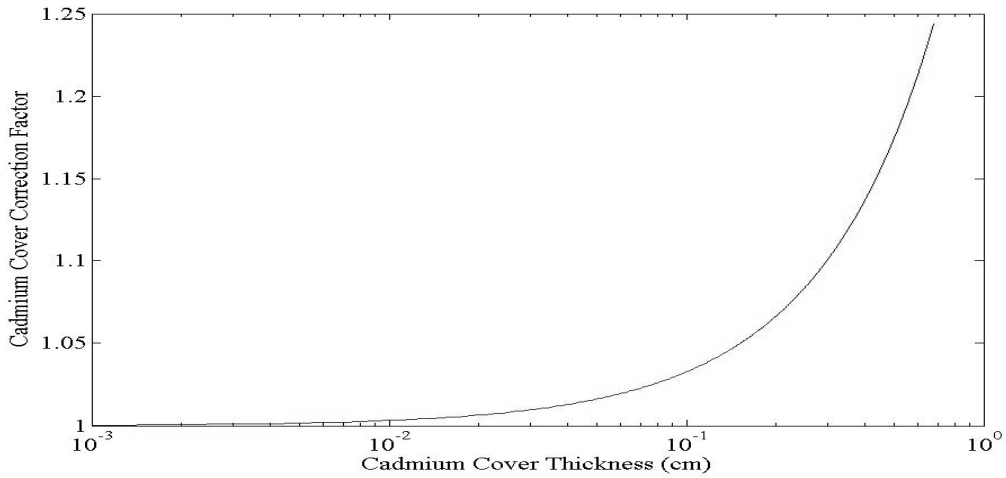

Figure 4.2. Epithermal correction factor F_{Cd} for a perpendicular neutron beam for varying Cd cover thickness.

4.1.2.3 Gold Self-Shielding and Flux-Density Depression Correction

Gold self-shielding *G* and flux-density depression *D* correction factors depend on the angular distribution of the neutron flux, foil size and thickness, and on the scattering and absorption cross-section of the surrounding material. For the neutron flux measurement conducted at the tangential beam port the angular distribution can be modeled as a perpendicular beam in air. For short distances, air can be considered a non-diffusing medium the neutron flux density depression factor is *D*=1, but the same argument cannot be applied to the gold self-shielding correction factor, *G*.

For the gold self-shielding correction factor, G, two components of the neutron flux must be considered: thermal neutron flux self-shielding factor G_t and fast neutron flux self shielding factor G_f.

The following assumptions are made for determining the thermal neutron flux self-shielding factor G_t: $\Sigma_a >> \Sigma_s$, the radius of the gold foil R is much greater than the thickness of the gold foil ($R >> d$), and the gold foil is irradiated by a perpendicular beam of thermal neutrons with a Maxwellian energy distribution whose value with depth x is given by

$$\varphi(x) = \varphi_s \exp\left(-\overline{\Sigma}_a x\right), \tag{4.25}$$

where φ_s is the thermal flux at the front surface of the foil, $\overline{\Sigma}_a$ is the average thermal macroscopic absorption cross section of the foil, and x is the distance into the foil [Shultis, 2002]. In thin gold foils there is negligible spectrum harding of the Maxwellian as neutrons pass through the gold foil, and the average macroscopic cross section is given by

$$\overline{\Sigma}_a = \frac{\sqrt{\pi}}{2}\Sigma_{ao} \tag{4.26}$$

and the thermal neutron flux self-shielding factor G_t is given by

$$G_t = \frac{1}{d}\int_o^d \exp\left(-\overline{\Sigma}_a x\right)dx\,. \tag{4.27}$$

One obtains

$$G_t = \frac{1}{\tau}(1 - e^{-\tau})\,, \tag{4.28}$$

where τ is given by [Shultis, 2002]

$$\tau = \overline{\Sigma}_a d\,. \tag{4.29}$$

For the epithermal neutron region, the absorption cross section has a *1/v* component and a resonant component that peaks at 4.91 eV with a peak value of σ_r = 30 kb. The *1/v* component is negligible compared to the resonance component. In this case, without significant Doppler broadening the fast neutron flux self-shielding factor for a thin foil without appreciable scattering can be approximated by

$$G_f = \left[I_0\left(\frac{\tau_r}{2}\right) + I_1\left(\frac{\tau_r}{2}\right)\right]\exp\left(-\frac{\tau_r}{2}\right), \tag{4.30}$$

where I_0 and I_1 are the modified Bessel functions of the first kind of the zeroth and first order, respectively, and τ_r is given by [Shultis, 2002]

$$\tau_r = \overline{\Sigma}_r d\ . \tag{4.31}$$

Applying the self-shielding correction factors, the fast neutron flux is given by

$$\varphi_f = \varphi_o \ln\left(\frac{E_{\max}}{E_{TC}}\right)\frac{1}{G_f} \tag{4.32}$$

and the thermal neutron flux is given by

$$\varphi_t = \left\{ \frac{A\left(\hat{R}_b - \hat{R}_c\right)}{N_a \overline{\sigma}_a} - \frac{\hat{R}_c A}{N_a I_r}\sqrt{\frac{16E_T}{\pi}}\left[\frac{1}{\sqrt{E_{TC}}} - \frac{1}{\sqrt{E_{CC}}}\right]\right\}\frac{1}{G_t}\,. \tag{4.33}$$

4.1.3 Gold Foil Activation Rates

Let $n(t)$ be the number of ^{198}Au atoms present in the gold foil. Then the rate of change of n is given by

$$\frac{dn}{dt} = m\hat{R} - \lambda n\,, \tag{4.34}$$

where λ is the decay constant of ^{198}Au and m is the mass of the gold foil. For the purpose of solving Eq. (4.34), it is assumed that no ^{198}Au atoms are present at $t = 0$. Then the number of ^{198}Au radionuclide daughters at a later time t is

$$n(t) = \frac{m\hat{R}}{\lambda}\left[1 - \exp\left(-\lambda t\right)\right]. \tag{4.35}$$

If the gold foil is kept in the neutron flux for a time much greater than the half-life of ^{198}Au, the activity will approach a saturation value $\lambda n_\infty = m\hat{R}$. After the gold foil is removed from the neutron flux at time t_1, the activity will exponentially decrease as

$$n(t) = n(t_1)\exp\left[-\lambda(t - t_1)\right], \tag{4.36}$$

and the activity is given by

$$\lambda n(t) = m\hat{R}\left[1 - \exp\left(-\lambda t\right)\right]\exp\left[-\lambda\left(t - t_1\right)\right]. \tag{4.37}$$

After the gold foil has been removed from the neutron flux the emitted radiation must be counted to determine $\hat{R}_b$ and $\hat{R}_c$. ^{198}Au emits a gamma ray of energy E = 411

keV with a frequency of f_e per decay, and is counted between times t_2 (the time the counting started), and t_3 (the time the counting stopped). If f_d is the Germanium detector absolute efficiency then the net total count is given by

$$C = \left(\frac{f_d \, f_e m \hat{R}}{\lambda} \right) [\exp(\lambda t_1) - 1][\exp(-\lambda t_2) - \exp(-\lambda t_3)]. \tag{4.38}$$

Solving Eq (4.38) for the equilibrium specific activation rate $\hat{R}$, we obtain

$$\hat{R} = \frac{\dfrac{\lambda C}{m f_d \, f_e}}{[\exp(\lambda t_1) - 1][\exp(-\lambda t_2) - \exp(-\lambda t_3)]}. \tag{4.39}$$

4.1.4 Gold Foil Irradiation Time Determination

Before the gold foil experiment can be conducted, the irradiation time for the gold foil at the tangential beam port must be determined. To determine the irradiation time t_1 the following equation was used

$$B = \frac{m N_a}{A} \sigma \varphi [1 - \exp(-\lambda t_1)], \tag{4.40}$$

where B is the desired emission rate. Solving Eq. (4.40) for t_1

$$t_1 = -\frac{\ln\left(1 - \dfrac{BA}{m N_a \sigma_a \varphi}\right)}{\lambda} \tag{4.41}$$

Table 4.1 contains the irradiation time for each of the gold foils, and the estimated neutron flux φ at tangential beam port for a reactor power of 500 kW. The estimated neutron flux was obtained from the Kansas State University TRIGA Mark II operation manual, which indicates that the flux in the tangential beam port is about 560 $cm^{-2} \, s^{-1} \, W^{-1}$. For an estimated neutron flux of $\varphi_t = 2.8 \times 10^8$ $cm^{-2} \, s^{-1}$ and a desired activity of 2.22×10^3 Bq the irradiation times for the bare and cadmium-covered gold foils are in given in Table 4.1.

Table 4.1. Gold foil irradiation times t_1

Gold Foil Sample	Gold Foil Mass m (g)	Irradiation Time t_1 (s)
A (bare)	0.0303	293
B (Cd covered)	0.0266	334

The actual irradiation times for the bare and Cd-covered gold foils at a reactor power of 500 kW was 430 s.

4.1.5 Gold Foil Activation Neutron Flux Measurement Uncertainty

The calculated neutron fluxes are subject to measurement uncertainty due to uncertainties in measured responses and in other parameters.

4.1.5.1 Thermal Neutron Flux Measurement Uncertainty

The thermal neutron flux uncertainty depends primarily on counting errors from the bare and cadmium covered foils. It can be assumed that there is negligible error associated with the mass of the gold foil, atomic mass, irradiation time, wait time before counting, count time, detector efficiency, reactor power, and cross sections. Then the standard deviation in the thermal neutron flux can be written as

$$\sigma(\varphi_t) = \left[\left(\frac{\partial \varphi_t}{\partial \hat{R}_b} \right)^2 \sigma^2(\hat{R}_b) + \left(\frac{\partial \varphi_t}{\partial \hat{R}_c} \right)^2 \sigma^2(\hat{R}_c) \right]^{1/2} . \tag{4.43}$$

The bare and Cd-covered activity uncertainty can be written as

$$\sigma(\hat{R}) = \left[\left(\frac{\partial \hat{R}}{\partial C} \right)^2 \sigma^2(C) \right]^{1/2} , \tag{4.44}$$

where $\frac{\partial \hat{R}}{\partial C}$ is determined from Eq. 4.39 and $\sigma^2(C)$ is the variance of the counts C given by $\sigma^2(C) = \sigma_G^2 + \sigma_B^2$, where σ_G is the gross counts uncertainty and σ_B is background counts uncertainty. The net counts uncertainty was given by the Genie 2000 software.

4.1.5.2 Fast Neutron Flux Uncertainty

The fast neutron flux uncertainty is given by

$$\sigma(\varphi_f) = \left[\left(\frac{\partial \varphi_f}{\partial \hat{R}_c} \right)^2 \sigma^2(\hat{R}_c) \right]^{1/2}, \tag{4.45}$$

where σ_f is given by Eq. (4.15) and

$$\sigma^2(\hat{R}_c) = \left(\frac{\partial \hat{R}_c}{\partial C_c} \right)^2 \sigma^2(C_c). \tag{4.46}$$

4.2 Gold Foil Activation Neutron Flux Measurement Results

The fast and thermal neutron fluxes were measured at the tangential beam port approximately 1 foot from the tangential beam port shutter at a reactor power of 500 kW, and the results are given in Tables 4.2, 4.3, and 4.4.

Table 4.2. Gold foil times

Gold Foil	Irradiation Time t_1 (s)	Count Start Time t_2 (s)	Count Stop Time t_3 (s)
A	430	2100	5703
B	430	9050	12,653

Table 4.3. Gold foil specific activation rates at a reactor power of 500 kW

Gold Foil	Net Counts C	Net Counts Uncertainty $\sigma(C)$	Bare Specific Activity R_b (Bq g^{-1})[1]	Covered Specific Activity R_c (Bq g^{-1})[1,2]	Standard Deviation $\sigma(\hat{R})$
A	18,464	159.88	3.14×10^{6}	-	2.72×10^{4} (0.87%)
B	2,874	73.46	-	5.81×10^{5}	1.48×10^{4} (2.55%)

[1]HpGe detector total detection efficiency was 4.45% for 411 keV gamma ray.

[2]For Cd cover thickness of 0.0508 cm F_{Cd}=1.02.

Table 4.4. Gold foil activation neutron flux measurement results at a reactor power of 500 kW

	Neutron Flux (cm^{-2} s^{-1})	% Uncertainty
Uncorrected Results		
φ_o	1.23×10^{5}	2.55
φ_f	2.17×10^{6}	2.55
φ_t	1.04×10^{7}	1.22
Normalized Uncorrected Results		
φ_f per W	20.0	2.55
φ_t per W	4.3	1.22
Gold Self-shielding Correction Factors		
G_f	0.909	-
G_t	0.989	-
Corrected Results		
φ_f	2.39×10^{6}	2.55
φ_t	1.05×10^{7}	1.22
Normalized Corrected Results		
φ_f per W	4.8	2.55
φ_t per W	21.0	1.22

4.2.1 Uncertainty Example Problem

The following is an example calculation of the uncertainties calculated for the thermal neutron flux in Tables 4.3 and 4.4. Substituting Eq. (4.16) into Eq. (4.43) for the thermal neutron flux φ_t yields the following for the thermal neutron flux uncertainty $\sigma(\varphi_t)$,

$$\sigma(\varphi_t)=\sqrt{\left(\frac{A}{N_a\bar{\sigma}_a}\right)^2\sigma^2\left(\hat{R}_b\right)+\left(\frac{-A}{N_a\bar{\sigma}_a}-\frac{A}{N_aI_r}\left[\sqrt{\frac{16E_T}{\pi}}\right]\left\{\frac{1}{\sqrt{E_{TC}}}-\frac{1}{\sqrt{E_{CC}}}\right\}\right)^2\sigma^2\left(\hat{R}_c\right)}, \quad (4.47)$$

where bare and Cd-covered specific activation rate uncertainties are given by

$$\sigma\left(\hat{R}_c\right)=\sqrt{\left(\frac{\frac{\lambda}{m_c f_d f_e}}{\left[\exp(\lambda t_1)-1\right]\left[\exp(-\lambda t_2)-\exp(-\lambda t_3)\right]}\right)^2 \sigma^2\left(C_c\right)} \tag{4.48}$$

and

$$\sigma\left(\hat{R}_b\right)=\sqrt{\left(\frac{\frac{\lambda}{m_b f_d f_e}}{\left[\exp(\lambda t_1)-1\right]\left[\exp(-\lambda t_2)-\exp(-\lambda t_3)\right]}\right)^2 \sigma^2\left(C_b\right)}. \tag{4.49}$$

The uncertainties for the bare foil net counts $\sigma(C_c)$ and Cd-covered foil net counts $\sigma(C_b)$ was given by the Genie 2000 software output and are given in Table 4.3. Substitute the values for each of the variables into Eqs. (4.47), (4.48), and (4.49) yields the uncertainty results contained in Tables 4.3 and 4.4.

Chapter 5 – HENDA System LLD Voltage Settings

Before HENDA performance testing could be conducted, the LLD voltage settings were determined in order to minimize detector system noise, i.e., to minimize the number of counts that are due simply to chance events rather than from charge that is due to a neutron interaction in the detector. Each HENDA has one LLD setting for the even channels and another LLD setting for the odd channels. The even and odd LLD voltage settings were set to 0.004 volts above the noise threshold for the most limiting even and odd channel, respectively.

5.1 HENDA System LLD Voltage Setting Testing

The detector system noise threshold first had to be determined. Knowing the HENDA system threshold ensures that the global LLD settings can be set to differentiate neutron interaction pulses from noise. The first part of the threshold experiment was to measure the threshold of the PATARA I chips only and the final part of the experiment was to measure the threshold of the PATARA I chips and the HENDA.

The LLD threshold occurs at the point where the detector and supporting components just fail to detect noise in the system without a neutron source present. The threshold for the odd channels was determined by stepping the odd global discriminator setting in increments of -0.004 volts while maintaining the even global LLD settings at a value where no even channel was counting. When the odd global LLD setting reached a value below a given odd channel's threshold, that channel began to produce count rates greater than a few thousand counts per second. As each odd channel threshold was reached, the voltage and the channel number were recorded. The odd global LLD setting was lowered until all the odd channel thresholds were determined. This process was repeated for the even global LLD voltage setting, while maintaining the odd global LLD voltage setting where the odd channels did not count.

5.2 Global LLD Voltage Settings Testing Results

The threshold noise levels of the system were determined under three conditions: first with no HENDA present; second with a planar device installed; and third with the 175-μm deep trenched device installed. This configuration determined the PATARA I

chip's threshold and the HENDAs' thresholds within the system, which helps the user to set the LLD to maximize neutron counts and minimize background noise.

5.2.1 PATARA I Chip LLD Voltage Setting

The LLD voltage settings for the PATARA I chips were determined without either HENDA installed in the system. Data were collected with the PATARA I chips in their normal locations and then the PATARA I chips were swapped (the top PATARA I chip was moved to the bottom PATARA I chip's location and the bottom PATARA I chip was moved to the top PATARA I chip's location). The LLD voltage setting was measured with the PATARA I chips in their normal locations by moving the LLD setting in -0.004 volt increments until an individual channel began to register counts. Then the PATARA I chip locations were swapped and the LLD voltage setting experiment was conducted for the swapped locations. The results of the test are given in Fig. 5.1. The reason that the test was conducted was to determine whether the non-uniform noise levels seen during LLD voltage testing were due to the PATARA I chips or to the supporting electrics on the motherboard. The results are plotted in Fig. 5.1. The LLD voltage setting remained fairly constant for the odd channels (at about -0.57 volts) for both positions of the PATARA I chips, and similarly for the even channels. Thus, it appears that the variation of the LLD voltage setting is a property of the PATARA I chips and not the supporting electronics.

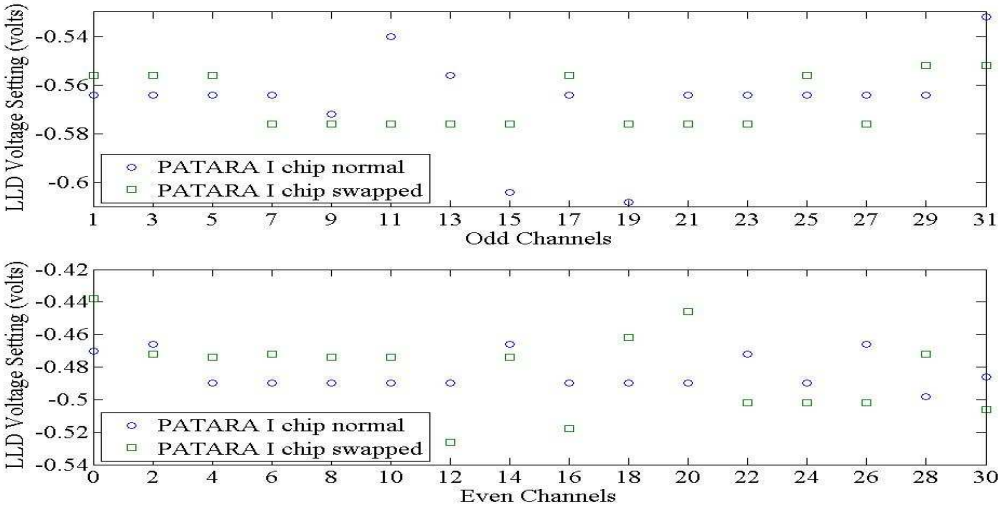

Figure 5.1. PATARA I chips LLD voltage settings for normal and swapped locations.

5.2.2 HENDA LLD Voltage Setting

The thresholds for the planar and trenched devices were also determined. As shown in Fig. 5.2 the LLD settings with the planar and trenched devices installed are just above the PATARA I chip LLD voltage settings. The small variation in LLD voltage settings for the PATARA I chips only between Figs. 5.1 and 5.2 may be due to the fact that the that data were collected on different days and the noise environment within the reactor bay may have been different, or may just be an indication of the extent of fluctuations. In any event, the data for the PATARA I chip are only are quite similar for the different tests.

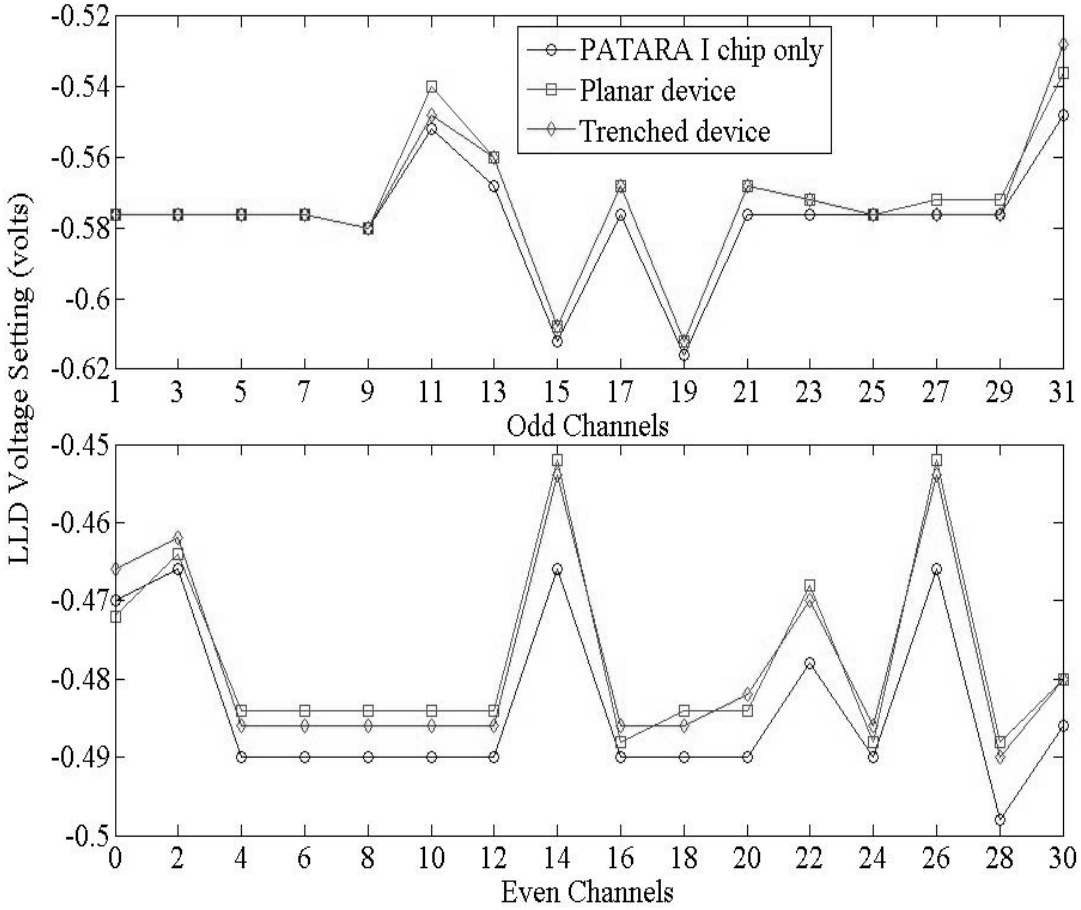

Figure 5.2. LLD voltage settings for the planar and 175-µm trenched devices compared to the PATARA I chips' LLD voltage settings.

The difference between the LLD thresholds for the planar and trenched devices and the LLD thresholds for the PATARA I chips only are plotted in Fig. 5.3. It is seen

that the noise introduced by the HENDAs is relatively small, reaching 20 mvolts in only one case.

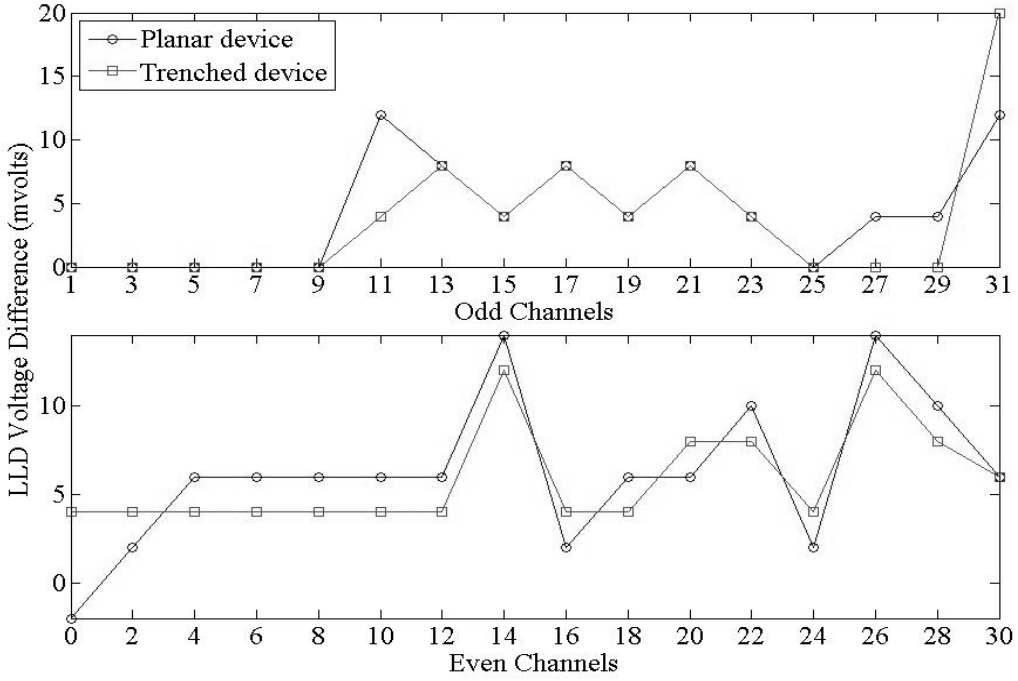

Figure 5.3. The difference in the LLD settings, from those for the empty PATARA I chip configuration, when the planar and trenched devices were installed.

The global LLD settings were determined for the odd and even channels to maximize the counts due to neutron interactions while minimizing counts from noise. From the results in Fig. 5.2, the most limiting channels for the planar device were 2, 14, 26, and 31. Thus, the planar device global LLD were set at -0.448 volts for the even channels and the -0.532 volts for the odd channels. For the 175-μm trenched device the limiting channels were also 2, 14, 26, and 31. Thus, the global LLD settings for the trenched device were set at -0.450 volts for the even channels and -0.522 volts for the odd channels. The 100-μm trenched device had similar limiting channels and global LLD setting as the planar device. The global LLD setting for the 100-μm trenched device was -0.448 volts for the even channels and -0.532 volts for the odd channels.

Chapter 6 – HENDA Performance Testing

HENDA performance testing was conducted at both the tangential beam port (southeast beam port) and the fast radial beam port (northwest beam port) located at the Kansas State University (KSU) TRIGA Mark II Reactor Facility. The major goals of the HENDA performance testing were to characterize the detector pulses due to neutron interactions, to investigate HENDA system dead time, to determine the spatial resolution of HENDA, to study HENDA counting uniformity, to study HENDA individual channel performance, and to estimate the neutron counting efficiency.

As shown in Fig. 6.1, the southeast beam port is oriented tangentially to the reactor core, with the near-core end of the tube in the graphite reflector [MNE, 2002]. The location of the beam tube with respect to the reactor core and reflector produces a beam having both thermal and epithermal neutrons. A 1-inch square collimator is used to narrow the beam. The tangential beam port was used to study the spatial resolution and neutron response/dead time of the detector. The northwest beam port is a radial tube that uses a graphite crystal to produce a diffracted neutron beam. Measuring neutron pulse heights, estimating channel uniformity and performance, and estimating thermal neutron counting efficiency for the HENDA were accomplished from the northwest beam port.

Performance testing was conducted on both planar and trenched HENDA devices. The trenched device came in two sizes: 175 μm and 100 μm deep trenches. The major difference between the 175-μm and 100-μm trenched devices was that the 100-μm trenched device used an aluminum trace around the perimeter of the trenches. The aluminum trace improves conduction of the collected charge to the bonding pads. It is noted that during the characterization of the HENDAs the KSU TRIGA Mark II reactor licensed power was upgraded from 250 kW to 1.25 MW. However, the upgrade did not affect the results of the HENDAs' characterization.

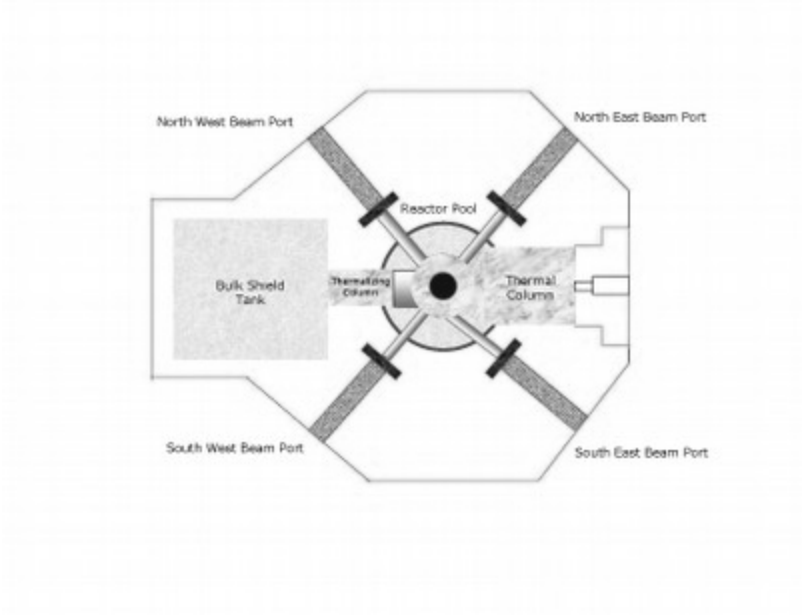

Figure 6.1. Horizontal section through the KSU TRIGA Mark II reactor [MNE, 2000].

6.1 HENDA Pulse Height Characterization Method and Results

An oscilloscope was used to display pulses due to neutron interactions. The neutron pulse height measurement was accomplished by soldering three contacts on the motherboard. Contacts where placed at the outputs of channels 4 and 27 of the PATARA I chips, and on a ground. Oscilloscope probes then were attached at one of the two channel contacts and to the ground and then AC coupled for the measurement of the neutron pulse heights. The pulse height measurements were taken at the diffracted beam, which is composed of mono-energetic thermal neutrons. From the pulse shapes one can estimate the pulse height, signal to noise ratio (SNR), rise time, fall time, total time, and noise level for the HENDA.

Pulse height measurements were made for the planar and 175-μm trenched devices, which provided an initial comparison of the two types of devices. As shown in Figs. 6.2 and 6.3, the pulse height measurements for the planar and trenched devices are quite similar.

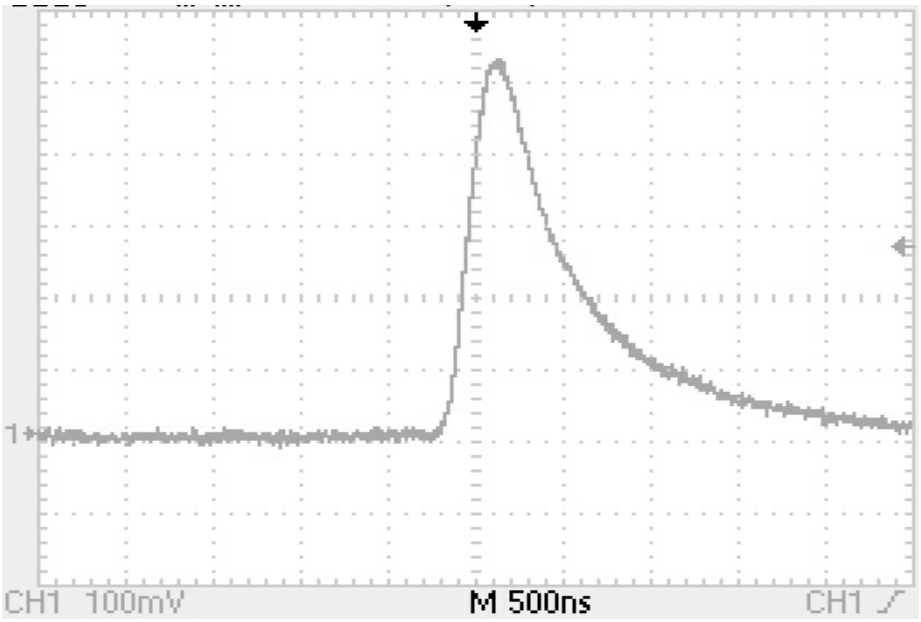

Figure 6.2. 175-µm trenched device pulse height measurement from PATARA I chip channel 27. Each block in the y-direction is 100 mV and in the x-direction is 500 ns. Oscilloscope settings; gain 100 mV, time constant 500 ns.

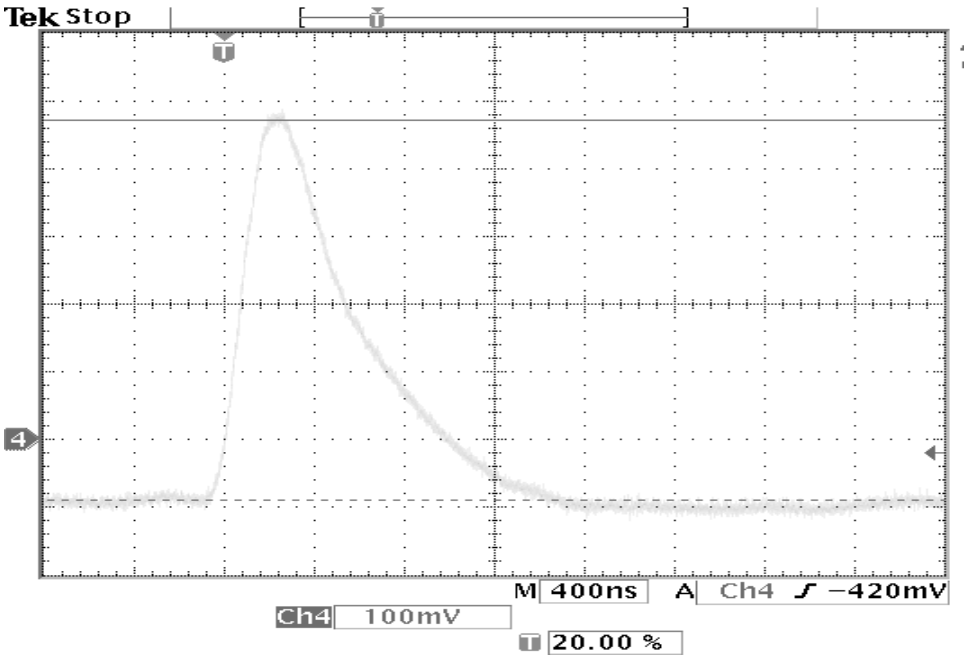

Figure 6.3. Planar device pulse height measurement from PATARA I chip channel 27. Each block in the y-direction is 100 mV and in the x-direction is 400 ns. Oscilloscope settings; gain 100 mV, time constant 400 ns.

Both devices had peak heights of between 500 and 600 mV, FWHM values of approximately 600 ns, and noise levels of about 13 mV. A more detailed examination of the pulses was accomplished by comparing signal to noise ratio (SNR), rise time, fall time, and total pulse duration, as shown in Table 6.1.

Table 6.1. HENDA pulse height measurement results

Detector	SNR	Rise Time (ns)	Fall Time (ns)	Total Duration (μs)
Planar	42:1	320	1240	1.5
100-μm trenched	42:1	200	1000	1.2
175-μm trenched	40:1	300	1800	2.1

6.2 HENDA System Dead Time

6.2.1 Experimental Method

The HENDA system dead time determination was conducted at the tangential beam port at reactor powers ranging from 2 kW to 512 kW. The dead time τ of the HENDA system is defined as the minimum time required to separate two pulses in order for both pulses to be counted as separate events [Knoll, 2000]. Two models for dead time are in common usage: paralyzable and non-paralyzable responses. The models represent the ideal behavior of a counting system and can be used to model a real counting system [Knoll, 2000]. The detector is assumed to be dead for a fixed time interval τ following each true event that occurs during the live period of the HENDA system. The events that occur during the dead time period of the HENDA system are lost and not counted as individual pulses.

In the non-paralyzable dead-time model, the fraction of all time that the detector is dead is given by $m\tau$, and thus the rate at which the true count rate is not counted by the HENDA system is $mn\tau$, where m is the measured count rate and n is the true count rate. This loss rate is just n-m and thus [see Knoll, 2000],

$$n - m = nm\tau \tag{6.1}$$

Solving for m, one obtains

$$m = \frac{n}{1 + n\tau}. \tag{6.2}$$

In the paralyzable case, the dead time period is not constant, therefore a non-paralzyable argument cannot be made. Instead the measured count rate *m* is identical to the rate of occurrences of the time intervals *T* between the true count rate *n* which exceeds the dead time τ. The distribution of the time intervals *T* between adjacent random events that occur at an average true count rate *n* is given by

$$P_1(T)dT = n\exp(-nT)dT, \tag{6.3}$$

where $P_1(T)dT$ is the probability of observing a time interval within dT about T [Knoll, 2000]. For probability intervals larger than τ, the probability can be obtained by integrating the distribution between τ and ∞, i.e,

$$P_2(\tau) = \int_0^{\infty} P_1(T)dT = \exp(-n\tau), \tag{6.4}$$

and the measured count rate *m* is obtained by multiplying Eq. (6.4) by the true count rate *n* giving the following equation for the measured count rate [Knoll, 2000]

$$m = n\exp(-n\tau). \tag{6.5}$$

As shown in Fig. 6.4 the major difference between the paralyzable model and the non-paralyzable model is the measured count rate achieves a maximum value and then decreases as the true count rate continues to increase for the paralyzable case. The determination of whether a detector system is a non-paralyzable or paralzyable detector is made by looking at the measured count rate vs. the true count rate. When the neutron count rate is low the two models give the same results; however at high neutron count rates the model results differ. For a non-paralyzable detector system at high count rate the measured count rate will approach an asymptotic value of $1/\tau$, representing the situation where the detector system barely has time to finish one dead time period before starting another. With a paralyzable detector system the observed rate goes through a maximum, and very high true count rates result in a multiple extension of the dead time period following the initial recorded count resulting in very few events being recorded by the detector system [Knoll, 2000].

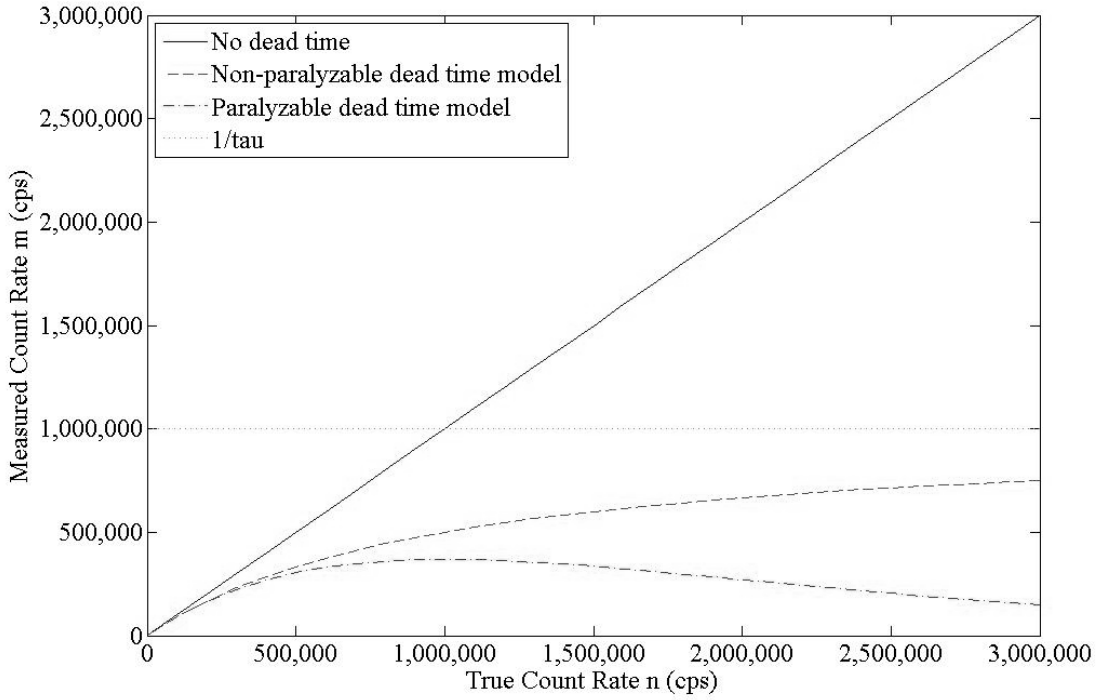

Figure 6.4. Measured count rate as a function of true count rate for the non-paralyzable and paralyzable dead time models.

6.2.2 Experimental Results

The response and dead time experiments were conducting concurrently for reactor powers ranging from 2 kW to 512 kW. A count time of 75 seconds was used for both the planar and 100 μm deep trenched devices. Each time reactor power was doubled the HENDA neutron count rate response should also double and have linear response if there is negligible dead time in the HENDA system. As shown in Fig. 6.5 the neutron counting response for both HENDAs tested was linear from 2 kW to 512 kW and the count rate for both devices approximately doubled for each change in reactor power as shown in Table 6.2. From the results in Fig. 6.5 and Table 6.2 it can be said that there is negligible dead time for both HENDAs operating in neutron flux levels of $\varphi \leq 1.08 \times 10^7$ cm^{-2} s^{-1}.

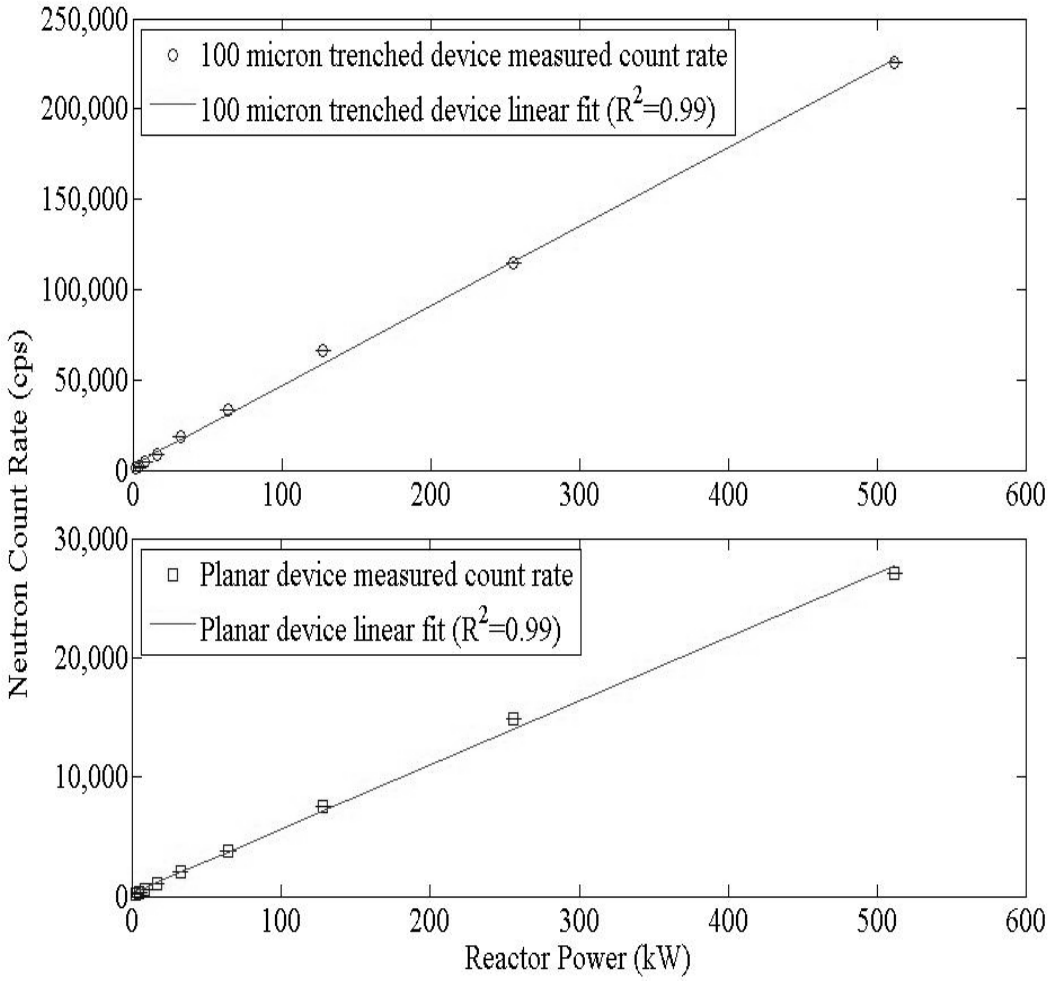

Figure 6.5. Planar and 100-µm trenched devices count rate from reactor power ranging from 2 kW to 512 kW.

Because the response is essentially proportional to the reactor power up to 512 kW it can be concluded that there is negligible dead time in the detector for a neutron flux up to 1.08×10^{7} cm^{-2} s^{-1} (see Table 6.2). Therefore, neither dead time model is needed to further characterize the detectors, and it can be concluded that the HENDAs can operate without dead-time losses at least up to flux levels of 10^{7} cm^{-2} s^{-1}.

Table 6.2. HENDA count rate response for reactor power ranging from 2 kW to 512 kW

Reactor Power (kW)	Neutron Flux φ (cm^{-2} s^{-1})	Count Rate (cps)	Multiplication Factor[1]
		Planar device	
2	4.21×10^{4}	143.73	-
4	8.41×10^{4}	291.27	2.02
8	1.68×10^{5}	541.83	1.86
16	3.36×10^{5}	1,031.53	1.90
32	6.73×10^{5}	2,048.61	1.99
64	1.35×10^{6}	3,812.53	1.86
128	2.69×10^{6}	7,578.72	1.99
256	5.38×10^{6}	14,864.07	1.96
512	1.08×10^{7}	27,113.93	1.82
		100-µm trenched device	
2	4.21×10^{4}	955.05	-
4	8.41×10^{4}	2,329.99	2.44
8	1.68×10^{5}	4,468.00	1.92
16	3.36×10^{5}	8,708.95	1.95
32	6.73×10^{5}	18,563.09	2.13
64	1.35×10^{6}	33,047.51	1.78
128	2.69×10^{6}	66,258.59	2.00
256	5.38×10^{6}	114,639.85	1.73
512	1.08×10^{7}	225,655.32	1.97

[1]Multiplication factor is the ratio of measured count rate at one power to that at the previous power, which was assumed to be half the current power. Reactor power may not have exactly doubled each time reactor power was raised because of limitations of reading the reactor power meters.

6.3 Confirmation of the HENDA Spatial Resolution

The spatial resolution of a detector array depends on the size of the individual detector channels. For the HENDA prototypes the size of each detector channel is 120 μm wide as described in Chapter one. Therefore, the spatial resolution of the HENDA prototypes should be 120 μm, to within the construction precision, which is presumed to be good. However, one can treat the HENDA as a detector with unknown resolution and conduct a knife-edge test (see below) to measure the resolution.

The spatial resolution for the planar detector array was confirmed by measuring the full-width at half maximum (FWMH) of the Line Spread Function (LSF), which is the first derivative of the Edge Spread Function (ESF) [Uher, 2005]. The ESF can be obtained by conducting a knife-edge test of the detector array. To conduct a knife-edge test, a sharp knife-edge, which covers a portion of the detector array is produced using a neutron absorbing material such as gadolinium (Gd), borated polyethylene, or cadmium (Cd) [Britton, 2004]. Regions of low and high total counts result. As shown in Fig. 6.6, the detector response is low over the region of the detector covered by the absorbing material and increases quickly to a high response region over the portion of the detector not covered by the absorbing material.

Counts obtained as the knife edge is moved relative to the detector can be used to produce a plot to which the ESF can be fitted. The ESF has the form

$$e(x) = a\,\mathrm{erf}[b(x-c)] + d\ , \tag{6.6}$$

where erf(x) is the error function, x is the incremental distance that HENDA traveled from the knife-edge, and a, b, c, and d are constants used to best fit Eq. (6.6) to the data. The LSF is given by the first derivative of the ESF [Uher, 2005] so that

$$l(x) = \frac{de(x)}{dx} = \frac{2ab}{\sqrt{\pi}}\exp\left[-b^2(x-c)^2\right], \tag{6.7}$$

and spatial resolution is then given by the FWHM of the LSF. The derivative of the error function is related to the Gaussian function and Eq. (6.7) is a Gaussian shape with a variance given by

$$\sigma^2 = \frac{1}{2b^2}\,. \tag{6.7a}$$

The FWHM of a Gaussian is given by

$$\text{FWHM} = 2\sqrt{2\ln(2)\sigma}\,, \tag{6.7b}$$

and thus the detector resolution is given by

$$\text{Resolution} = \text{FWHM} = \frac{2\sqrt{\ln(2)}}{b}\,. \tag{6.7c}$$

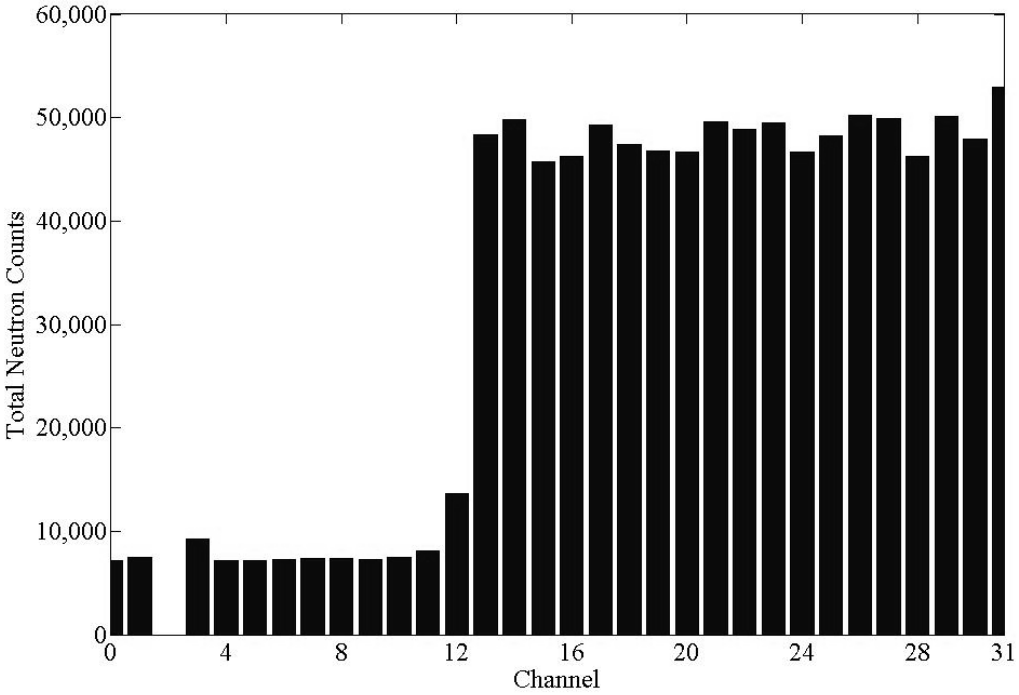

Figure 6.6. Data collected with knife-edge aligned near channel 12 of the planar device.

For the purpose of conducting this experiment, Gd evaporated onto a silicon wafer, made by the SMART lab, was used for the knife-edge test. As shown in Fig. 6.7, Gd has a very large neutron absorption cross-section at thermal energies. Thus, only a very small amount of Gd is required to make the knife-edge. Use of Gd ensures a sharp edge to minimize neutron scattering, which occurs when using thicker layer of neutron absorbing material such as borated polyethylene or Cd. The Gd-covered device is shown in Fig 6.8.

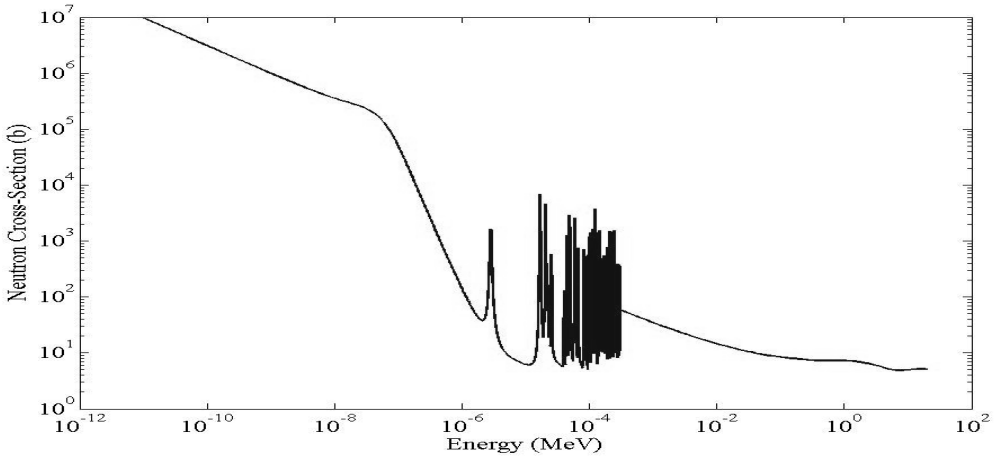

Figure 6.7. Absorption cross-section versus neutron energy for ^{157}Gd reaction [Brookhaven, 2006].

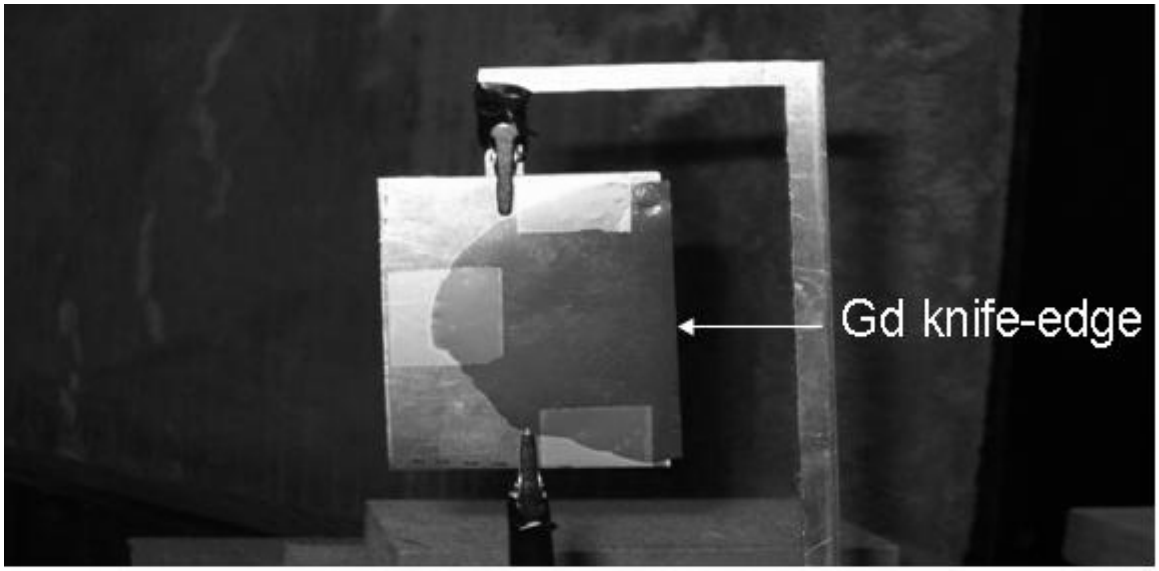

Figure 6.8. The thin aluminum substrate onto which the gadolinium was deposited is suspended between clamps. The gadolinium has a straight knife edge on the right, as shown. The silicon wafer is not shown.

Prior to conducting the knife-edge test for a given detector array the LLDs should be set to ensure neutron count rates of the channels are approximately equal. The odd and even LLDs were set at -0.368 volts and -0.380 volts, respectively, to achieve neutron count rates that differed by 5% or less among the channels, expect for channel two, as shown in Fig. 6.9. After the LLDs had been set, the knife-edge alignment was verified. If the knife-edge was not parallel with the HENDA it could give an incorrect spatial resolution for the HENDA. As shown in Fig. 6.6 when the knife-edge is aligned parallel

with the detector a very clear distinction between the low and high end counts can be achieved.

The knife-edge test was conducted at the tangential beam port at a reactor power of 100 kW with a counting time of 5 minutes using the Gd knife-edge on a silicon wafer. The Gd knife-edge remained stationary and the HENDA was moved 250 μm, a little over two channel widths, in 25-μm increments using a translation stage to obtain data to determine the ESF. Thus, depending on where the knife-edge was originally located, three or four channels could be affected by the 250 μm movement. Each time the HENDA was translated an additional portion of some channel was further covered causing the covered channel counts to decrease, as shown in Fig. 6.9. It appears that, initially, almost all of channel 11, but not quite all, was covered by the Gd knife-edge because on Run01 the counts are slightly higher than for all the other runs. Note that channel 2 was unresponsive and that channels 12 through 14 were the ones affected by the knife-edge movement. The results shown in Fig. 6.9 indicate that the knife-edge initially (Run 01) partially covered channel 12, and eventually passed entirely through channel 13, and ended up (Run 10) partially covering channel 14.

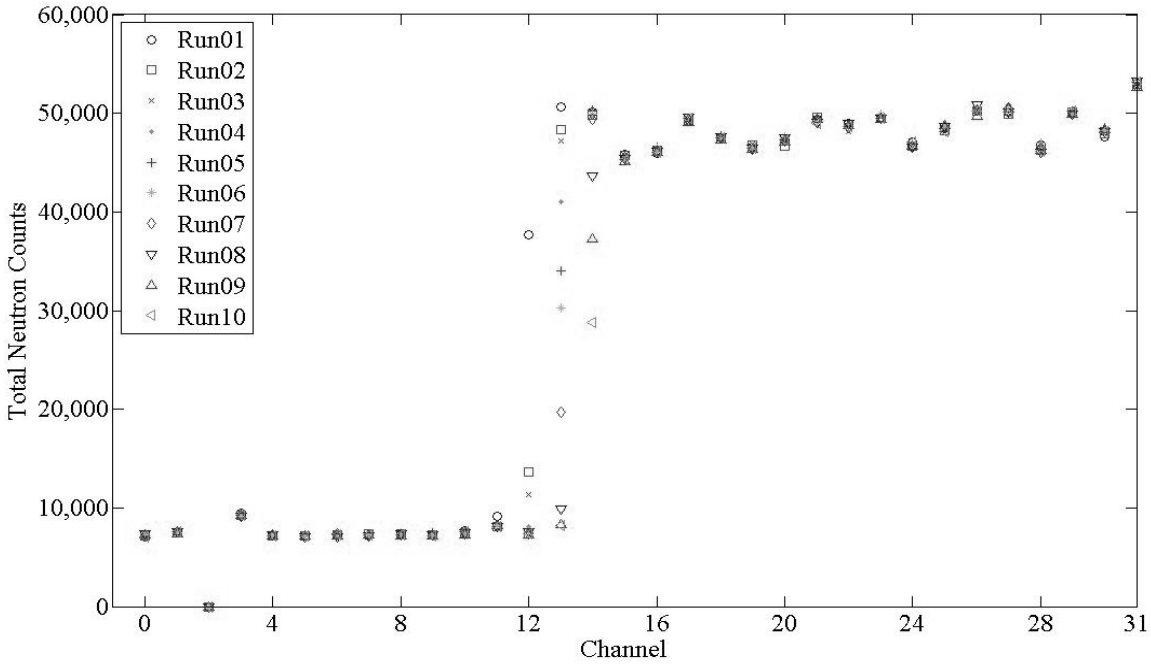

Figure 6.9. The total neutron counts for versus channel for each of the 10 data runs for the planar device.

Fig. 6.9 shows how individual channels responded during the movement of the HENDA relative to the Gd knife-edge, but it was difficult to determine the ESF directly from the data shown in Fig. 6.9. Therefore, the data were re-plotted to distinctly show the channel response as the Gd knife-edge covered a channel. Thus, channel 13 data were used to determine the ESF. The results for channel 13 as a function of the displacement of the knife edge as shown in Fig. 6.9. From amount the HENDA was translated with respect to the stationary Gd knife-edge the ESF can now be determined, as shown in Fig 6.10. The ESF constants were determined by fitting Eq. (6.6) to the data points shown in Fig. 6.10 for the total length of 250 μm that the planar device was translated relative to the knife-edge. After the ESF model constants were determined, they can be substituted into Eq. (6.7) to obtain the LSF, as shown in Fig. 6.10. Given *b*, the spatial resolution was estimated to be 122.6 μm, in good agreement with the known resolution of 120 μm.

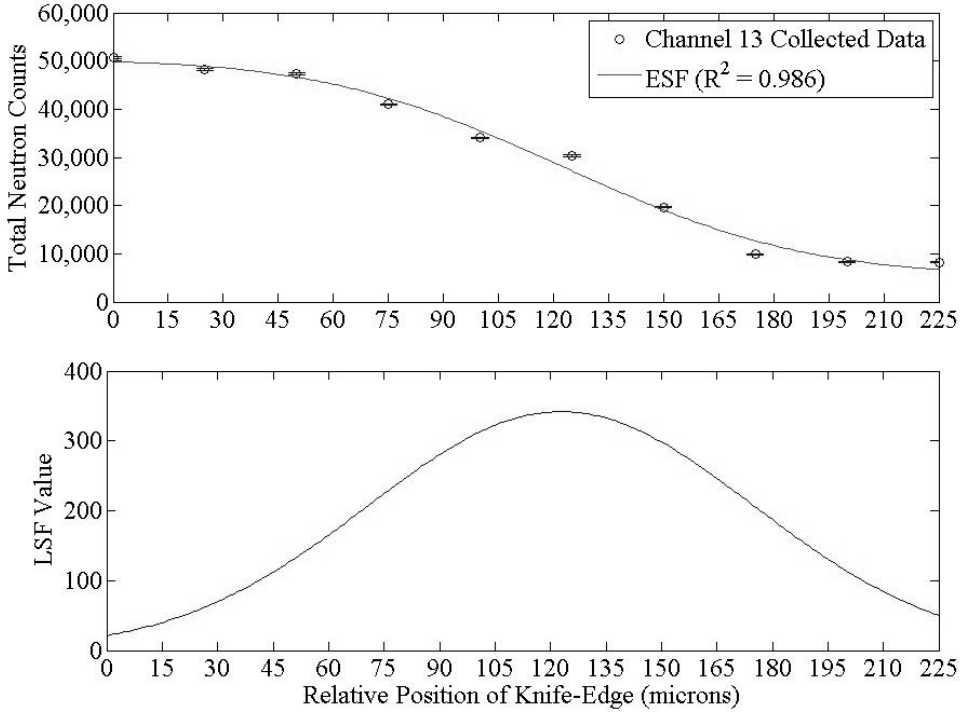

Figure 6.10. The Planar device's ESF and LSF determined by displacing of the HENDA with respect to the GD knife-edge in 25 μm increments.

Table 6.3. Model fits constants for the ESF and LSF for the planar device

Model	a	b	c	d	Model Fit R^2
ERF fit	22,300	0.01358	122.8	27,950	0.986

The spatial resolution of the planar and 100-μm trenched devices was also confirmed during a visit to Oak Ridge National Laboratory (ORNL) for the initial demonstration of the HENDA. During the demonstration of the HENDA at the High Flux Isotope Reactor (HFIR), a 300 μm slit in a beryllium target was used to further demonstrate the spatial resolution of the HENDA. From the known planar device's spatial resolution, the number of channels that should be counting neutrons was approximately three. The data for the planar and the 100-μm trenched devices are shown in Figs. 6.11 and 6.12. The distance from the slit to the detector was not minimized causing some beam divergence resulting in additional channels that were counting. Additionally, channel 3 of the planar device registered counts this was due to the fact that multiple beam lines where in use during the demonstration at HFIR resulting in a high neutron background.

The 100-μm trenched device had similar results to the planar device, as shown in Fig. 6.12. From that comparison it can be said that the 100-μm trenched and the planar devices have similar spatial resolutions. Thus, the spatial resolution for the 100-μm trenched device was also determined to be approximately 120 μm.

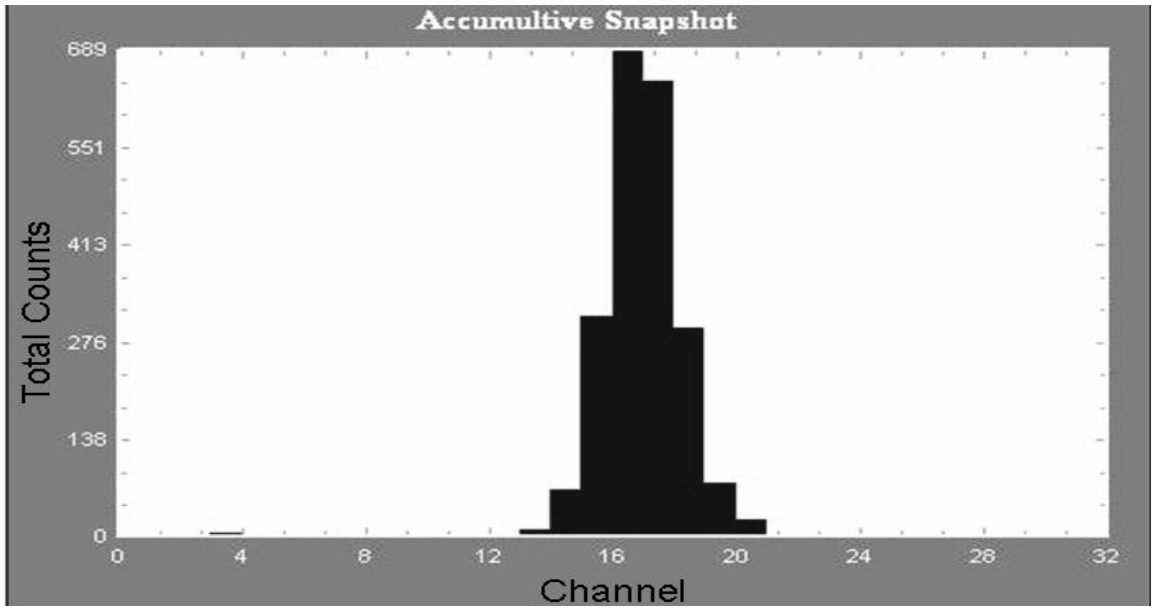

Figure 6.11. Planar device response when aligned with a 300 μm beryllium slit during ORNL HFIR demonstration of HENDA.

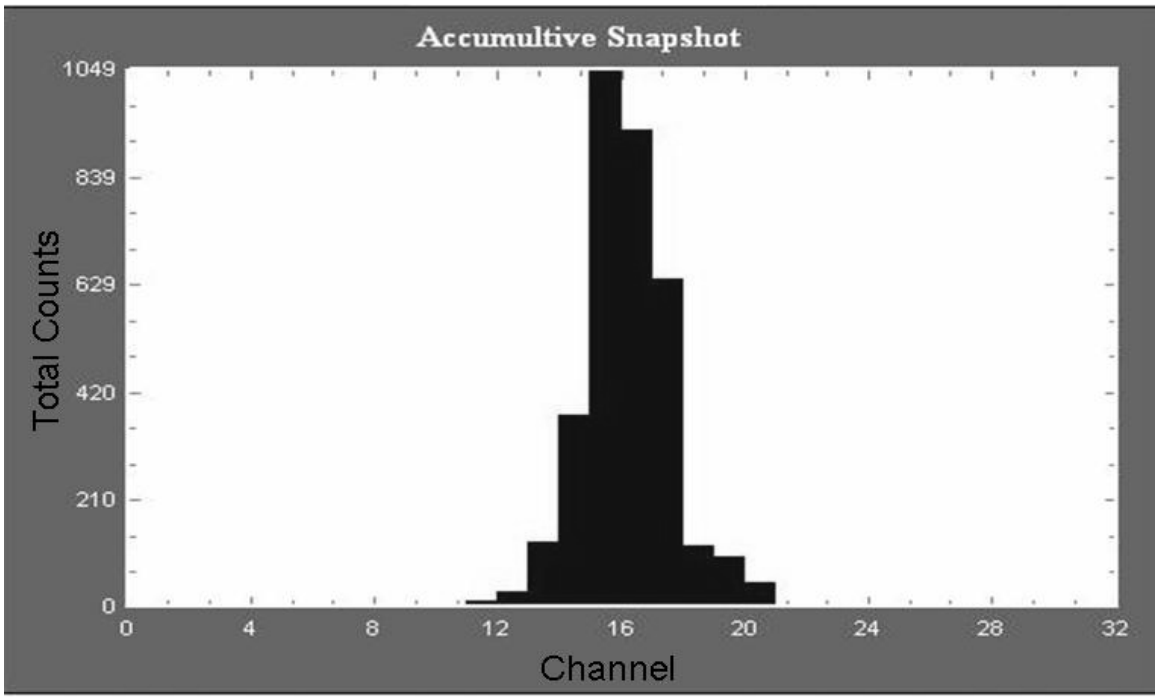

Figure 6.12. 100-m trenched device response when aligned with a 300 μm beryllium slit during ORLN HFIR demonstration of HENDA.

The 120-μm spatial resolution of both devices was further confirmed during a study of the counting efficiency. The devices were placed in front of a 2.54 cm thick BC_4 block that contained a 1.5 mm diameter hole, which ensured the neutron beam was

smaller than each device. From the 122 μm spatial resolution the number of channels that should be counting was 13 channels for both devices. Data collected for both devices are shown in Fig. 6.13. This once again demonstrates that the 100-μm trenched and planar devices have similar spatial resolutions of 120 μm. The reason for the variation of counts among the channels can be contributed to the PATARA I chips. There was only two LLD setting for the HENDA system, one for the even channels and one for the odd channels. With the global LLD settings set to the most limiting odd and even channel, the voltage threshold required for a given channel to record a count varied among the channels. Given that not every neutron interaction produces the same amount of charge collection causing varying pulse height voltage. Having different LLD voltage thresholds for each channel and varying pulse height voltage due to neutron interactions caused the data scatter among the channels.

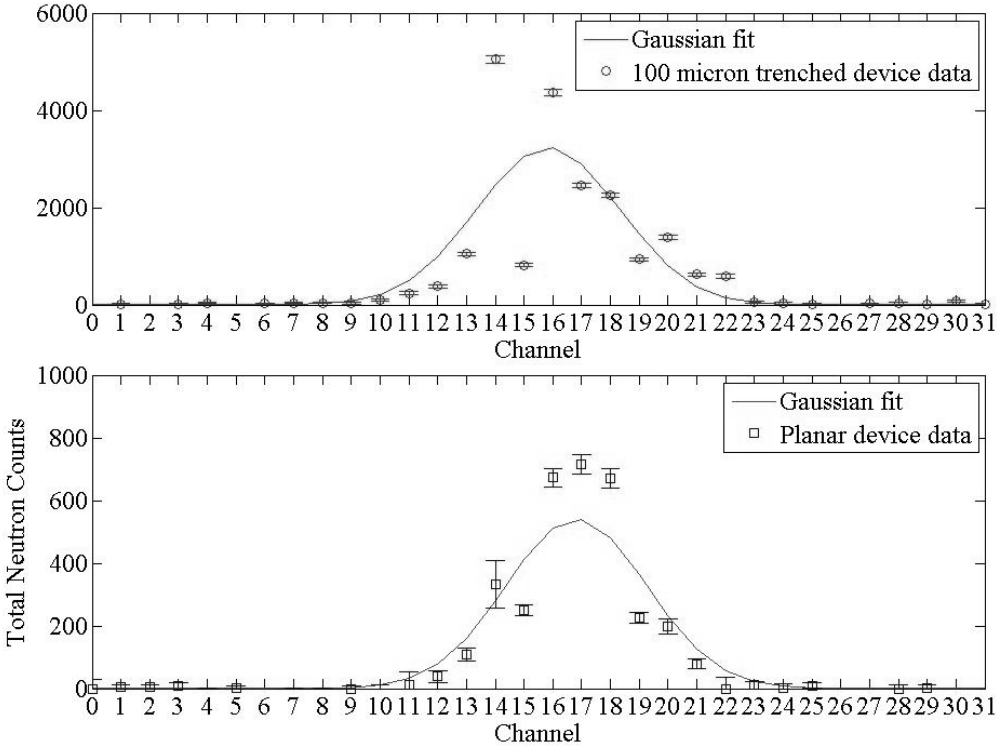

Figure 6.13. Response from both the 100-μm trenched and planar devices aligned with the beam from a 1.5mm diameter BC_4 collimator.

6.4 HENDA Counting Uniformity Method and Results

The HENDA uniformity testing was performed at the diffracted neutron beam. To conduct the uniformity test, a modification to the HENDA system mount was made. The HENDA system mount was rotated 90 degrees to allow the HENDA to be placed horizontally in the diffracted neutron beam, as shown in Fig. 6.14. The diffracted neutron beam was chosen due to the small diameter (1.27 cm) of the neutron beam, which allows small areas of the HENDA to be exposed to the neutron beam. The count rate obtained for each area exposed to the neutron beam can be determined and tracked by translation stage position.

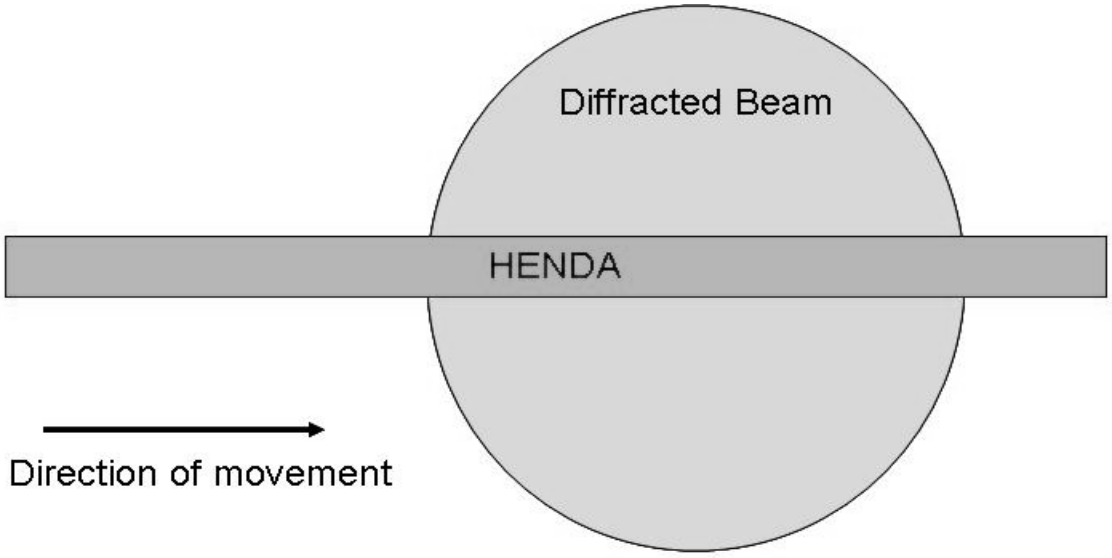

Figure 6.14. HENDA alignment within the diffracted beam for the neutron counting uniformity experiment.

The uniformity test was conducted on both trenched devices and on the planar device. The difference between the 175-μm and 100-μm trenched device was that a thin aluminum trace on the perimeter of the trenches was used in the 100-μm trenched device to lower the resistance to allow charge to move more freely through the detector to the bond pads. As shown in Fig. 6.15, without the aluminum trace present, the 175-μm trenched device does not have a uniform neutron counting response across the length of the detector. The planar device, on the other hand does have a have uniform neutron counting response across the length of the detector, presumably because of the aluminum metal trace on the perimeter of each channel. The neutron count rate is lower at the

edges, because the 1.27 cm diameter neutron beam did not fully cover either device when it was less than 1.27 cm from an edge.

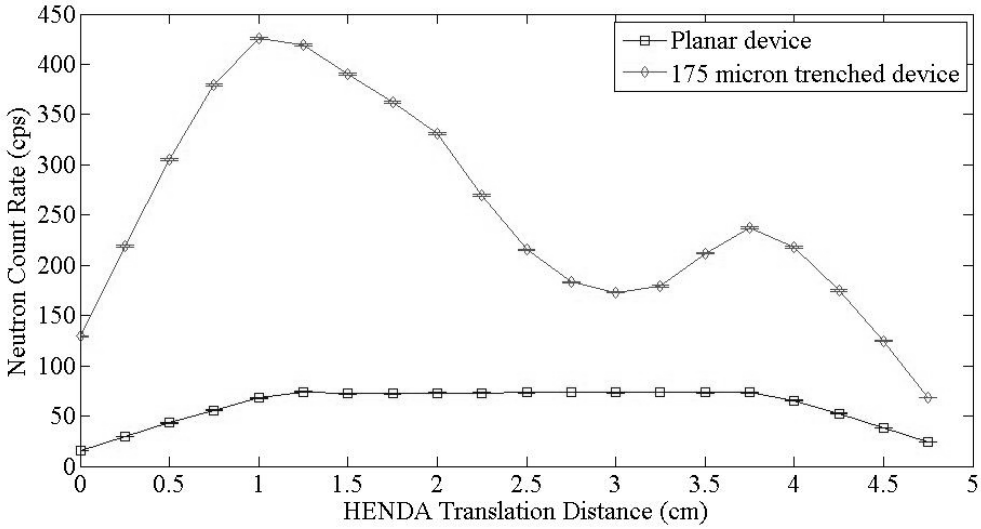

Figure 6.15. Uniformity test results for the planar and 175-μm trenched devices conducted prior to KSU TRIGA Mark II reactor power upgrade.

As the 175-μm trenched device was translated through the diffracted neutron beam, odd and even channel uniformity was studied. As shown in Fig. 6.16, the even channels were responsible for the total neutron count rate when the neutron beam was close to the even channels' bonding pads (0 to 3 cm). As the neutron beam moved across the length of the 175-μm trenched device, moving toward the odd channel bonding pads, the count rate for the even channels was reduced and the count rate for the odd channels began to rise as the neutron beam moved closer to the odd channel's bonding pads. At 3 cm the count rates from the odd and even channels were approximately equal, and after 3 cm the odd channels were responsible for most of the total neutron count rate since the neutron beam was closer to the odd channels' bonding pads. The aluminum metal trace on the perimeter of the 100-μm trench device's trenches made its neutron counting response more uniform across the length of the detector, as shown in Fig. 6.17. From Fig. 6.17, it is seen that the neutron counting efficiency for the 100-μm trenched device is approximately 9 to 10 times that of the planar device.

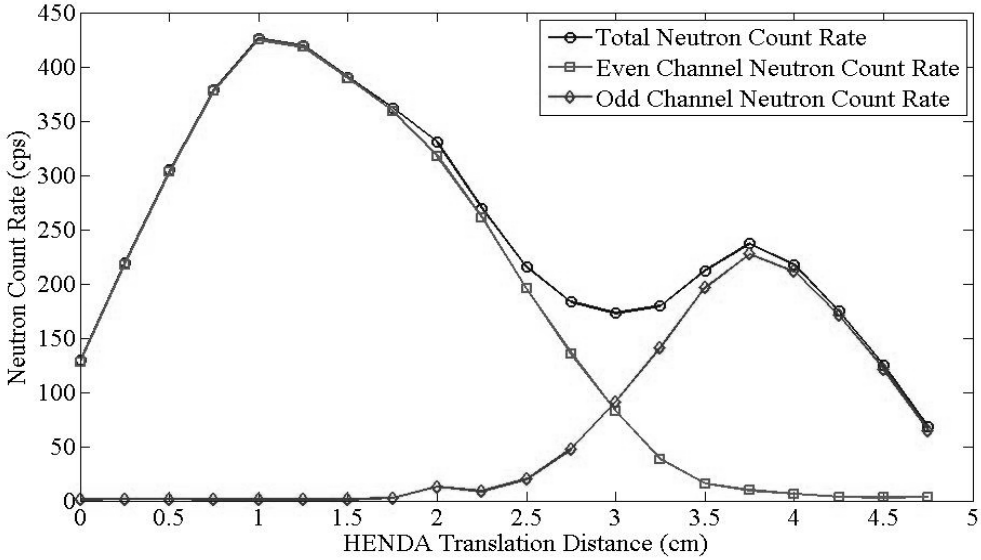

Figure 6.16. 175-µm trenched device's odd and even channels count rate compared to the 175-µm trenched device's total neutron count rate.

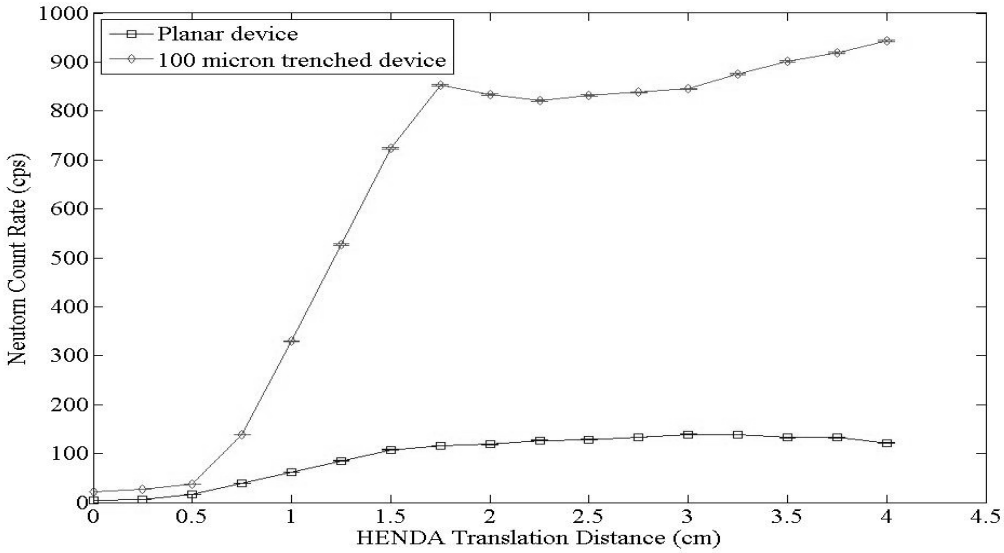

Figure 6.17. Uniformity test results for the planar and 100-µm trenched devices conducted after KSU TRIGA Mark II reactor power upgrade.

6.5 HENDA Individual Channel Performance Method and Results

The individual channel performance was determined by translating the HENDA through the diffracted beam in small increments. At each position *x* the total counts for

each individual channel and the overall total counts from all 32 channels were recorded. The HENDA was oriented in its normal configuration, as seen in Fig 3.2, with no additional collimation of the diffracted beam. For each position *x* the data were saved to a text file, which provided a record of the total counts for each channel at each position *x*. Let $f_i(x)$ be the counts recorded by channel *i* when the HENDA was at position *x* and let $g(x)$ be the overall total counts from all 32 channels when the HENDA was at position *x*, i.e. $g(x) = \sum_{i=0}^{31} f_i(x)$. Then the individual Channel Performance Ratio (CPR_i) is given by

$$\mathrm{CPR}_i = \frac{g(x)}{f_i(x)}, i = 0,1,2,...,31. \tag{6.8}$$

The CPR_i provided a method of determining how an individual channel is performing with respect to the overall HENDA performance. The more uniform the various CPR_i values are, the better is the performance of the HENDA. If a channel is not counting, then $f_i(x) = 0$ CPR_i goes infinite. Furthermore, the CPR_i cannot be zero unless $g(x)=0$, which can only happen if none of the channels are counting. In an ideal case of zero noise level and uniform response of the channels, the CPR would be 32 for each channel.

The CPR was determined for the planar and 100-μm trenched devices using the 1.27 cm diameter diffracted neutron beam, and the odd and even global LLD were set to allow for the maximum number of neutron counts. Reactor power was at 100 kW and the counting time was 150 seconds. The devices were moved across the diffracted neutron beam in 13 increments of 0.175 cm each. The detailed data are given in Appendix A and the total, channel 0, channel 16, and channel 31 counts for the both HENDA devices are plotted in Figs 6.18 and 6.19 versus HENDA position, as measured from an arbitrary starting position. Channel 0 represents the left end of the array, channel 16 represents the middle of the array, and channel 31 represents the right end of the array.

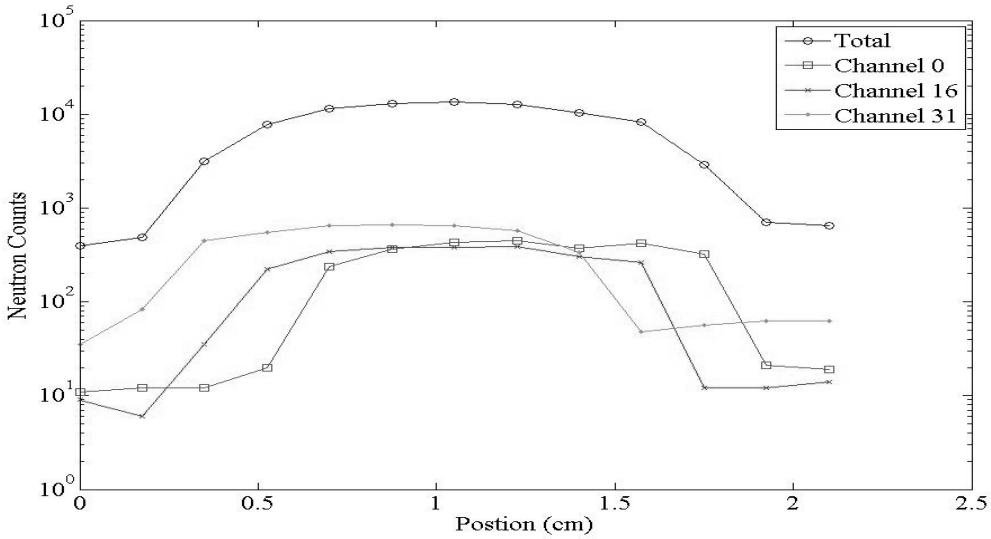

Figure 6.18. Planar devices neutron counts profile of the 1.27 cm diameter diffracted beam at a reactor power of 100 kW. The planar device was orientated in the beam as shown in Fig. 3.2. The planar was translated through the non-collimated diffracted beam in 13 increments of 0.175 cm. The total is $g(x)$ and the individual channels are $f_i(x)$.

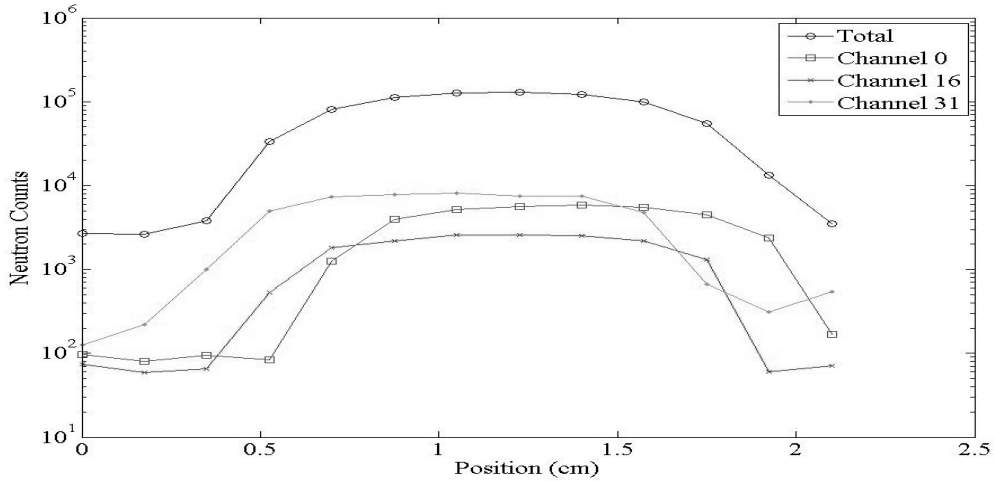

Figure 6.19. 100-µm trenched device neutron counts profile of the 1.27 cm diameter diffracted beam at a reactor power of 100 kW. The 100-µm trenched device was orientated in the beam as shown in Fig. 3.2. The 100-µm trenched device was translated through the non-collimated diffracted beam in 13 increments of 0.175 cm. The total is $g(x)$ and the individual channels are $f_i(x)$.Where the total is $g(x)$ and the individual channels are $f_i(x)$.

The x positions that where used to determine $g(x)$ and $f_i(x)$ for the planar device were x = 0.7 cm to 1.4 cm and for the 100-μm trenched device were x = 0.875 cm to 1.575 cm. Given the x positions, $g(x)$, and $f_i(x)$ are know and Eq. (6.8) can be applied to determine the channel performance ratio for 32-channels for the 100-μm trenched and planar devices. The CPR results are shown in Figs. 6.20 and 6.21 and Appendix A provides $g(x)$ and $f_i(x)$ values. As seen from the results of the individual channel performance ratio there is a correlation between PATARA I chip thresholds and channel performance. The CPR does not just measure the detector channel performance, but the entire system individual channel performance. Knowing the individual channel performance will allow users to set the LLD according to the experiment that will be conducted. If the experiment requires high efficiency the odd and even global LLDs can be set at just above the noise level, or if a uniform counting among channels is required the odd and even global LLDs can be adjusted to lower count rate for the even or odd channels to obtain the results shown in Figs. 6.6 and 6.9.

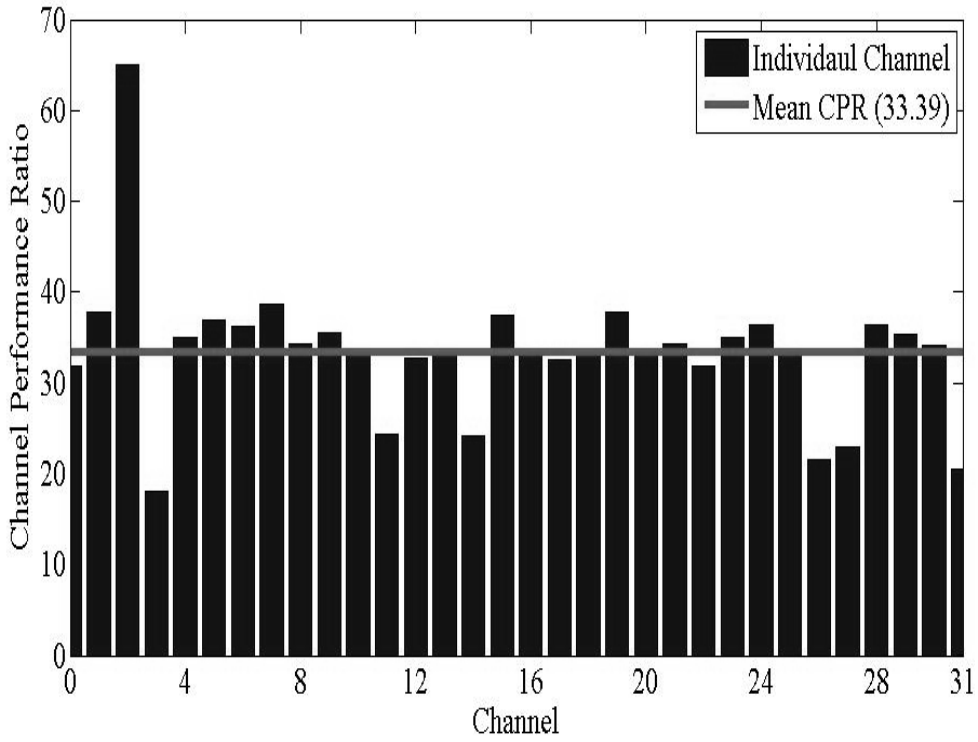

Figure 6.20. Planar device individual channel performance ratio with a mean CPR of 33.39.

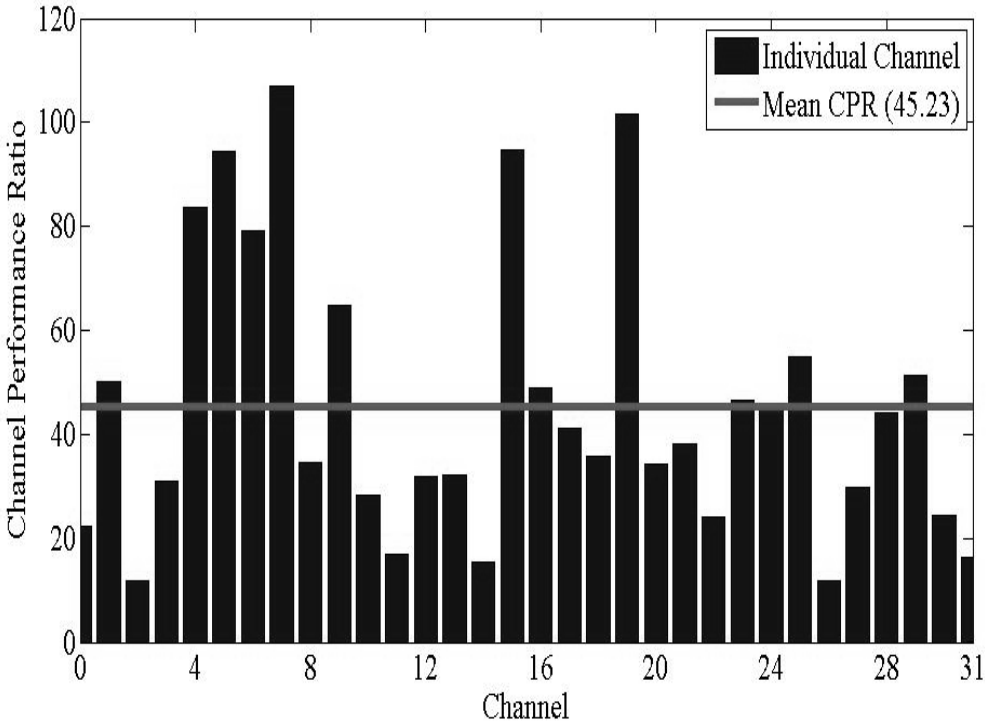

Figure 6.21. 100-μm trenched device individual channel performance ratio with a mean CPR of 45.23.

For the 100-μm trenched device the variation of the CPR was also due to the PATARA I chip's non-uniform baseline and the non-uniform packing of trenches with ^{6}LiF powder from channel to channel. The non-uniform packing of ^{6}LiF powder can explain why the mean $CPR_{100\ \mu m\ trenched\ device}$ > mean $CPR_{planar\ device}$.

6.6 HENDA Neutron Detection Efficiency Method and Results

The HENDA neutron counting efficiency was determined by using a mono-energetic neutron flux from the diffracted neutron beam at the northwest beam port of the KSU TRIGA Mark II reactor. The mono-energetic beam allowed the determination of the neutron counting efficiency for thermal neutrons only.

6.6.1 HENDA Collimator Lineup and LLD Settings

The 1.5 mm diameter collimator was made using a $2.54 \times 2.54 \times 2.54$ cm BC_4 block. The collimation was accomplished by drilling a 1.5 mm diameter hole through the center of the BC_4 block. The HENDA was placed in front of the collimator with minimal

distance between the two, the divergence of the neutron beam was minimal and therefore negligible. The HENDA was then aligned to the 1.5 mm diameter hole by translating the array until 13 channels were counting. The number of channels that would be counting due to the collimator was obtained by dividing the 1.5 mm diameter hole by the spatial resolution of the HENDA (120 μm).

The LLD settings do have an effect on neutron counting efficiency. If the LLD settings were too high, neutron counts would be missed and the neutron counting efficiency would be reduced. If the LLD settings are too low then the neutron counting efficiency could be overestimated due to counting electronic noise. The global odd and even LLDs were set approximately 4 mvolts above the LLD for the noisiest odd and even channels, respectively. With those LLD settings, it was observed with no neutron flux present no pulses where recorded by the HENDA system. This ensured the neutron counting efficiency was not overestimated.

6.6.2 Thermal Neutron Beam Rate and Neutron Detection Efficiency Determination

The thermal neutron beam rate was determined using a ^{3}He detector that was placed in front of the collimator with minimal distance between the detector and collimator. The minimal distance ensured that beam divergence was negligible, and therefore would not have to be accounted for when determining the HENDA neutron counting efficiency. The thermal neutron beam rate determination was conducted at a reactor power of 200 kW and the counting time was set to ensure totals counts greater than 10,000 counts leading to 1% or less statistical error. The measured net neutron count rate for the ^{3}He detector was determined by the following equation

$$m_{He-3} = m_{He-3,shutter\ open} - m_{He-3,shutter\ closed}, \tag{6.9}$$

where $m_{He\text{-}3,shutter\ open}$ is the measured neutron count rate with the diffracted beam shutter open and $m_{He\text{-}3,\ shutter\ closed}$ is the measured neutron count rate with the diffracted beam shutter closed. The measured neutron count rate with the shutter closed was due to residual neutron background counts during reactor operation such as neutrons being emitted from the diffracted beam shielding.

The HENDA neutron counting efficiency was determined by a two part experiment at a reactor power of 200 kW at a counting time to ensure that the total counts

are 10,000 or greater leading to 1% or less counting error. The net neutron count rate *m* for the HENDA was determined by

$$m = m_{shutter\ open} - m_{shutter\ closed}\,. \tag{6.10}$$

6.6.3 Neutron Detection Efficiency Experimental Results

The major difference between the planar and 100-μm trenched device was in the CPR and the neutron counting efficiency (ε). From the other experiments that were conducted one can see that the neutron counting efficiency for the 100-μm trenched should be approximately 10 times that of the planar device neutron counting efficiency.

6.6.3.1 Relative Neutron Detection Efficiency

The neutron counting efficiencies for the planar and 100-μm trenched device were determined at a reactor power of 200 kW. Tables 6.4 and 6.5 provides the data that were collected for the neutron counting efficiency of the planar and trenched devices and is compared to the results from a GE Reuter-Stokes ^{3}He detector, model number RS-P4-1602-207. Because the mono-energetic neutron energy of the diffracted beam was not exactly known at the time the neutron counting efficiency experiment was conducted, the efficiencies of the HENDAs can only be specified in terms of the ^{3}He neutron detector, i.e. $\varepsilon_{\text{relative}} = \dfrac{m}{m_{\text{He}-3}}$. Therefore the neutron counting efficiencies for the planar and 100-μm trenched devices were determined to be 1.45% and 15.02% of the ^{3}He detector, respectively. This is consistent with the other experiments that were conducted to characterize the HENDA prototypes the neutron counting efficiency of the 100-μm trenched device should be approximately 10 times the neutron counting efficiency of the planar device. Assuming the thermal neutrons were at the most probable energy of 0.0253 eV and the ^{3}He detector efficiency was 83.5% at that energy, the efficiencies of the planar and 100-μm trenched devices would be 1.21% and 12.54%, respectively. The neutron detection efficiency data for the ^{3}He detector was provided by the manufacture GE Reuter-Stokes.

Table 6.4. Relative neutron detection efficiency data and results for the planar device

Detector	Counting Time *t* (s)	Total Counts Shutter Open	Total Counts Shutter Closed	Net Count Rate (cps)	Relative Neutron Detection Efficiency (%)
^{3}He	900	86,797	51,584	39.13±0.41	-
Planar	3000	7096	5396	0.57±0.037	1.45±0.095

Table 6.5. Relative neutron detection efficiency data and results for the 100-μm trenched device

Detector	Counting Time *t* (s)	Total Counts Shutter Open	Total Counts Shutter Closed	Net Count Rate (cps)	Relative Neutron Detection Efficiency (%)
^{3}He	300	71,872	12,582	197.63±0.97	-
Trenched	2000	64,452	-	29.69±0.14	15.02±0.10
Trenched	600	-	1510	-	-

The uncertainty for the relative neutron counting efficiency is given by

$$\frac{\sigma_{\varepsilon}}{\varepsilon} = \sqrt{\left(\frac{\sigma_{He-3\ net\ counts\ rates}}{m_{He-3}}\right)^2 + \left(\frac{\sigma(m)}{m}\right)^2}\ , \qquad (6.11)$$

where $\sigma_{He-3\ net\ count\ rate} = \sqrt{\left(\sqrt{\frac{m_{He-3\ shutter\ open}}{t}}\right)^2 + \left(\sqrt{\frac{m_{He-3\ shutter\ closed}}{t}}\right)^2}$ and

$$\sigma(m) = \sqrt{\left(\sqrt{\frac{m_{HENDA\ shutter\ open}}{t}}\right)^2 + \left(\sqrt{\frac{m_{HENDA\ shutter\ closed}}{t}}\right)^2}\ .$$

6.6.3.1 Neutron Detection Efficiency Equation

In order to demonstrate the HENDAs' efficiency variation with respect to energy, the analysis from Chapter two was revisited. We do not know the ^{3}He detector's neutron counting efficiency at the time the neutron counting efficiency experiment was conducted, because we do not know the neutron energy of the diffracted beam. However, presuming that the neutron energy of *E=0.0253* eV for the diffracted beam being the most probable thermal neutron energy one would obtain the following results. Given the experimental data from Tables 6.4 and 6.5 and the above assumption the experimental neutron counting efficiency equation for the 100-μm trenched and planar devices can be determined. The experimental neutron counting efficiency for the planar and 100-μm trenched devices can be determined from the following two equations that where derived in Chapter two, for the planar device

$$\varepsilon_{planar}(E) = C_p(d)\{1-\exp[-aN\sigma_a(E)d]\} \tag{6.12}$$

and for the 100-μm trenched device

$$\begin{aligned}\varepsilon_{trench}(E) &= C_{t_1}(d)\frac{w-w_t}{w}\{1-\exp[-aN\sigma_a(E)d]\} \\ &+ C_{t_2}(d,D)\frac{w_t}{w}\{1-\exp[-aN\sigma_a(E)(d+D)]\}\end{aligned} \tag{6.13}$$

.

For the given HENDAs the variable *d* and *D* are fixed and thus Cp and Ct are constants. To determine these constants, the ^{3}He neutron counting efficiencies must be known. From the manufacture's data, the ^{3}He neutron detector efficiency for neutron energy *E*=0.0253 eV, was 83.50%, and the experimental neutron counting efficiency for the HENDAs is given by $\varepsilon_{\text{experimental}} = \varepsilon_{\text{relative}}\varepsilon_{\text{He}-3}$. The constant can be determined from the results shown in Table 6.6.

Table 6.6. Neutron detection efficiency for a neutron energy *E*=0.0253 eV

Detector	Calculated Maximum Neutron Detection Efficiency (%)	Experimental Neutron Detection Efficiency (%)	Constant C_{t1}	Constant C_{t2}	Constant C
Planar	2.79	1.21±0.095	-	-	0.43
100-μm trenched	12.84	12.54±0.10	0.1284	1.5786	-

Substituting the constant *C* into Eqs. (6.12) and (6.13) the neutron counting efficiency equation for the planar device is given by

$$\varepsilon_{planar}(E) = 0.43\{1-\exp[-aN\sigma_a(E)d]\} \tag{6.14}$$

and for the 100-μm trenched device

$$\begin{aligned}\varepsilon_{100-\mu m\ trench}(E) &= C_{t_1}(d)\frac{w-w_t}{w}\{1-\exp[-aN\sigma_a(E)d]\} \\ &+ C_{t_2}(d,D)\frac{w_t}{w}\{1-\exp[-aN\sigma_a(E)(d+D)]\}\end{aligned}. \tag{6.15}$$

Finally the HENDAs' relative neutron counting efficiency with respect to the ^{3}He neutron detector for the planar device is given by

$$\varepsilon_{planar,relative}(E) = \frac{0.43}{\varepsilon_{\mathrm{He-3}}(E)}\{1-\exp[-aN\sigma_a(E)d]\} \tag{6.16}$$

and for the 100-μm trenched device

$$\begin{aligned}\varepsilon_{100-\mu m\ trench,relative}(E) &= \frac{0.1284}{\varepsilon_{\mathrm{He-3}}(E)}\frac{w-w_t}{w}\{1-\exp[-aN\sigma_a(E)d]\} \\ &+ \frac{1.5786}{\varepsilon_{\mathrm{He-3}}(E)}\frac{w_t}{w}\{1-\exp[-aN\sigma_a(E)(d+D)]\}\end{aligned}, \tag{6.17}$$

and the results are shown in Fig. 6.22.

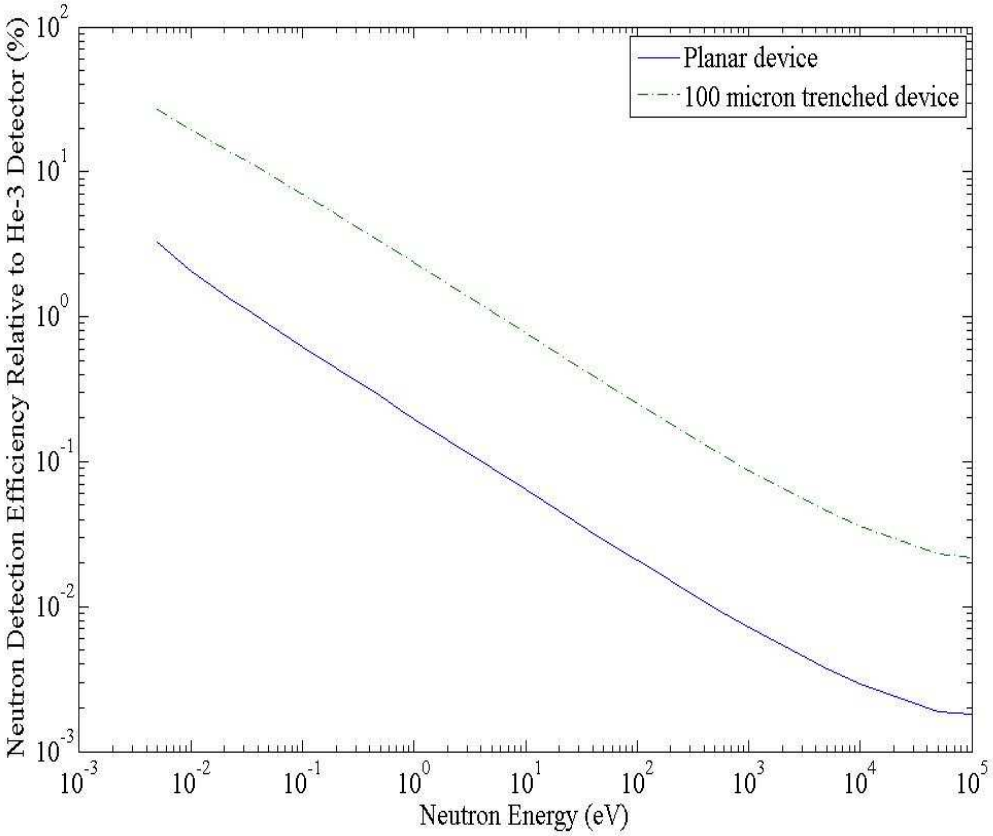

Figure 6.22. Planar and 100-µm trenched devices' neutron detection efficiency relative to the ^{3}He neutron detector from Eq. (6.16) and Eq. (6.17). The neutron detection efficiency for the ^{3}He detector was obtained from GE-Reuter Stokes.

Chapter 7 – Conclusion

The HENDA prototype has met the design specification set by the Spallation Neutron Source and by the initial proposal submitted by KSU SMART Lab. The spatial resolution of 120 μm was within the 100 to 500 μm goal. The prototypes have relatively fast response times, with pulse durations on the order of 1-2 μs. The neutron detection efficiency goal of 50% can be obtained by using deeper trenches and using a sandwich design, and the HENDAs are insensitive to gamma rays. The added benefit of the HENDA system is that at neutron fluxes $< 10^7$ cm^{-2} s^{-1}, which are seen at HFIR and SNS experiments, the HENDA systems had negligible dead times. With HENDA's spatial resolution, response time, and neutron counting efficiency, future HENDAs will be valuable neutron detector systems to be used for neutron diffraction experiments. The spatial resolution of 120 μm will allow scientists to investigate materials using neutrons with sub-mm resolution. It will provide a better understanding of the residual stresses in materials and molecular structure of a given material or crystal structure. Individual HENDAs or HENDA arrays will enable new experiments in neutron diffraction and imaging.

When the planar and 100-μm trenched devices are compared, the 100-μm trench device has a distinct advantage over the planar device in terms of neutron counting efficiency and response time, but the two devices have similar neutron counting response and dead time. From the characterization of the planar and the 175-μm and 100-μm trenched devices, there were distinct differences among the HENDAs. It was founded that an aluminum metal trace was useful in improving charge collection. If no aluminum trace was present the HENDA's response was non-uniform, as shown with the 175-μm trenched devices.

The planar and 100-μm trenched devices have similar spatial resolutions (120 μm) and neutron counting response for varying neutron fluxes showed the HENDAs had negligible dead time for neutron fluxes $\varphi \leq 10^7$ cm^{-2} s^{-1}. Both devices were affected by the non-uniform baseline threshold of the PATARA I chips as shown in the individual CPR results, but there was an added effect for the 100-μm trenched device due to the non-uniform ^{6}LiF packaging among the individual trenches. The major difference and clear advantage of the 100-μm trenched device over the planar device was the neutron

detection efficiency. The 100-μm trenched device efficiency was 15% of the ^{3}He detector whereas the planar was about 1.5% of the ^{3}He detector, making the 100-μm trench device approximately 10 times more efficient than the planar device.

During the completion of this thesis a 1024-channel HENDA array, and supporting electronics was under development. This array, based on the 100-μm trenched device prototype is planned to be used at SNS for material science studies using neutron diffraction. Additionally, the 32-channel 100-μm trenched device is being used at HFIR to show that HENDA can be used for neutron diffraction experiments.

7.1 Future Work

From the results obtained during the characterization of the HENDA prototypes, future work should focus on neutron diffraction experiments. Given the sub-mm resolution of the HENDA prototypes this is a valid next step in demonstrating the effeteness of using the HENDA prototypes in material science research. ORNL already has ongoing material science research being conducted at HFIR, such as the Neutron Powder Diffraction and Neutron Residual Stress Mapping Facility. The sub-mm resolution of the HENDA prototypes would be ideal for the above experiments and would be beneficial in material science research.

References

Argonne National Laboratory, "Reactor Physics Constants," ANL-5800, U.S. Government Printing Office, Washington DC, 1963.

Brookhaven National Laboratory, "Evaluated Nuclear Data File (ENDF)," http://www.nndc.bnl.gov/exfor7/endf00.htm, December 15, 2006.

Britton Jr., C.L, Bryan, W.L., Wintenberg, A.L., Warmack, R.J., McKnight, T.E., Frank, S.S., Copper, R.G., Dudney, N.J., Veith, G.M., Stephan, A.C. "A Detector for Neutron Imaging," IEEE, 2004.

Britton, J.L., Bunch, S.C. , Britton Jr., C.L. , Blalock, B.J. , McGregor, D.S., Crow, L. "Patara: Solid-State Neutron Detector Readout Electronics with Pole-Zero and Complex Shaping and Gate Baseline Restorer for SNS", IEEE Nuclear Science Symposium Conference 2006.

Chakoumakos, Bryan "Instrument HB-2A High Flux Isotope Reactor – Neutron Powder Diffractometer," Oak Ridge National Laboratory, http://neutrons.ornl.gov/hfir_instruments_systems/HB-2A.shtml, 2008.

Cottingham, W.N. and Greenwood, D.A. "Introduction to Nuclear Physics," Cambridge University Press, 2001, 2nd edition.

Department of Mechanical and Nuclear Engineering (MNE), "Safety Analysis Report," Kansas State University TRIGA Mark II Nuclear Reactor Facility, License R-88 Docket 50-188, 11 September 2002.

Duderstadt, J.J. and Hamilton, L.J. "Nuclear Reactor Analysis," John Wiley and Sons, Inc, 1976.

Dunn, W.L., Jahan, Q.M., McGregor, D.S., McNeil, W.J., Patterson, E.L., Rice, B.B., Shultis, J.K., Soloman, C.J., 2007. Design and performance of a portable neutron dosimeter, Proceedings of the 2nd Workshop on European Collaboration for Higher Education and Research in Nuclear Engineering and Radiological Protection, 13-15 March, 2006, Valencia, Spain, pp. 85-92.

Faw, R.E., and Shultis, J.K., "Radiological Assessment: Sources and Exposure", PTR Prentince-Hall Inc, 1993.

Hubbard, Camden "Instrument HB-2B High Flux Isotope Reactor – Neutron Residual Stress Mapping Facility," Oak Ridge National Laboratory, http://neutrons.ornl.gov/hfir_instruments_systems/HB-2B.shtml, 2008.

Knoll, G.F. "Detection and Measurement", John Wiley and Son, Inc, 2000, 3rd Edition.

Jahan, Q., Patterson, E., Rice, R., Dunn, W.L., McGregor D.S., 2007. Neutron dosimeters employing high-efficiency perforated semiconductors, Nucl. Instrum. and Meth. in Phys. Res. B 263(1), 183-185.

Lamarsh, J.R. "Introduction to Nuclear Reactor Theory," American Nuclear Society, 2002.

McGregor, D., Bellinger, S.L., Bruno, D., Dunn, W.L., McNeil, W.J. Patterson, E. Rice, B.B., Shultis, J.K., Unruh T. 2009. Perforated diode neutron detector modules fabricated from high-purity silicon. Radiat. Phys. Chem. (in press).

McGregor, D.S. "IMR-MIP/High-Detection-Efficiency and High-Spitial-Resolution Thermal Neutron Imaging System for the Spallation Neutron Source and using Pixelated Semiconductor Neutron Detectors," 2007 Status Report to NSF for NSF contract DMR0412208, Kansas State University, Department of Mechanical and Nuclear Engineering, September 2007.

McGregor, D.S., Hammig, M.D, Yang, Y.-H., Gersch, H.K., Klann, R.T. "Design considerations for thin film coated semiconductor thermal neutron detectors-I: basics regarding alpha particle emitting neutron reactive films", Nuclear Instruments and Methods in Physics Research Section A Volume 500, 2003, pg 272-308.

McNeil, W.J, Bellinger, S.L., Blalock, B.J., Britton Jr., C.L., Britton, J.L., Bunch, S.C., Cowley, S.A., Henderson, C.M., Sobering, T.J., Taylor, R.D., McGregor, D.S. "Preliminary Tests of a High Efficiency 1-D Silicon Pixel Array for Small Angle Neutron Scattering." IEEE Nuclear Science Symposium Conference, 2007.

Shultis, J.K. "Measurement of Thermal and Fast Neutron Fluxes by Gold Foil Activation," Rev. 2, NE648 Spring 2002, Kansas Sate University, unpublished.

Spallation Neutron Source, “Instrument Systems Data Acquisition System Overview,” Oak Ridge National Laboratory, September 2004, Draft.

Turner, J.E. “Atoms, Radiation, and Radiation Protection”, John Wiley and Son, Inc, 1995, 2nd edition.

Uher, J., Holy, T., Jakubek, J., Lehmann, E., Pospisil, S., Vacik, J. “Performance of a pixel detector suited for slow neutrons,” Nuclear Instruments and Methods in Physics Research Section A, Volume 542, pg 283-7, 2005.

Appendix A – $g(x)$ and $f_i(x)$ values for the Planar and 100-µm Trenched Devices

The $g(x)$ and $f_i(x)$ for the planar and 100-µm trenched devices are provided in Tables A.1, A.2, and A.3. The CPR for channel i was determined from the data contained in Tables A.1, A.2, and A.3 and using Eq. 6.8.

We will use channel 0 of the planar as an example of how the CPR was calculated for each channel of the HENDA prototypes, as shown in Tables A.2 and A.3. For the planar device $g(x)$ = [11,438 at x = 0.700; 12,910 at x = 0.875; 13,438 at x = 1.050; 12,663 at x = 1.225; 10,365 at x = 1.400] and $f_{channel\ 0}(x)$ = [235 at x = 0.700; 367 at x = 0.875; 427 at x = 1.050; 446 at x = 1.225; 376 at x = 1.400], which is in the format of a 1×4 matrix. Eq. 6.8 can now be rewritten as $f_{channel\ 0}(x)\mathrm{CPR}_{\mathrm{channel\ 0}} = g(x)$. Solving $\mathrm{CPR}_{\mathrm{channel\ 0}}$ using Gaussian Elimination we find that the $\mathrm{CPR}_{\mathrm{channel\ 0}}$ = 31.87.

Table A.1. $g(x)$ values for the Planar and 100-µm trenched device

Detector	x (cm)	$g(x)$ (counts)
Planar device	0.700	11,438
	0.875	12,910
	1.050	13,438
	1.225	12,663
	1.400	10,365
100-µm trenched device	0.875	112,542
	1.050	126,908
	1.225	129,095
	1.400	123,087
	1.575	100,367

Table A.2. Planar device values for $f_i(x)$ and Channel Performance Ratio (CPR)

Channel, *i*	*x* (cm)	$f_i(x)$ (counts)	CPR
	0.700	235	
	0.875	367	
0	1.050	427	31.87
	1.225	446	
	1.400	376	
	0.700	206	
	0.875	294	
1	1.050	348	37.87
	1.225	346	
	1.400	362	
	0.700	102	
	0.875	176	
2	1.050	192	65.08
	1.225	222	
	1.400	200	
	0.700	628	
	0.875	721	
3	1.050	730	18.13
	1.225	700	
	1.400	577	
	0.700	219	
	0.875	331	
4	1.050	404	35.00
	1.225	366	
	1.400	368	

Table A.2. (cont.) Planar device values for $f_i(x)$ and Channel Performance Ratio (CPR)

Channel, *i*	*x* (cm)	$f_i(x)$ (counts)	CPR
	0.700	247	
	0.875	339	
5	1.050	355	36.93
	1.225	329	
	1.400	356	
	0.700	272	
	0.875	335	
6	1.050	395	36.16
	1.225	351	
	1.400	318	
	0.700	264	
	0.875	335	
7	1.050	350	38.64
	1.225	326	
	1.400	295	
	0.700	280	
	0.875	318	
8	1.050	368	34.22
	1.225	389	
	1.400	343	
	0.700	280	
	0.875	318	
9	1.050	368	35.51
	1.225	389	
	1.400	343	

Table A.2. (cont.) Planar device values for $f_i(x)$ and Channel Performance Ratio (CPR)

Channel, *i*	*x* (cm)	$f_i(x)$ (counts)	CPR
	0.700	316	
	0.875	377	
10	1.050	393	33.47
	1.225	390	
	1.400	340	
	0.700	462	
	0.875	492	
11	1.050	542	24.34
	1.225	551	
	1.400	451	
	0.700	360	
	0.875	376	
12	1.050	404	32.71
	1.225	387	
	1.400	335	
	0.700	336	
	0.875	358	
13	1.050	398	33.65
	1.225	388	
	1.400	328	
	0.700	461	
	0.875	509	
14	1.050	581	24.13
	1.225	508	
	1.400	459	

Table A.2. (cont.) Planar device values for $f_i(x)$ and Channel Performance Ratio (CPR)

Channel, *i*	*x* (cm)	$f_i(x)$ (counts)	CPR
	0.700	299	
	0.875	323	
15	1.050	365	37.43
	1.225	306	
	1.400	328	
	0.700	344	
	0.875	378	
16	1.050	384	33.85
	1.225	389	
	1.400	301	
	0.700	357	
	0.875	401	
17	1.050	399	32.69
	1.225	371	
	1.400	339	
	0.700	351	
	0.875	406	
18	1.050	380	32.62
	1.225	373	
	1.400	339	
	0.700	295	
	0.875	354	
19	1.050	345	37.75
	1.225	332	
	1.400	285	

Table A.2. (cont.) Planar device values for $f_i(x)$ and Channel Performance Ratio (CPR)

Channel, *i*	*x* (cm)	$f_i(x)$ (counts)	CPR
	0.700	360	
	0.875	361	
20	1.050	437	33.25
	1.225	356	
	1.400	307	
	0.700	338	
	0.875	360	
21	1.050	392	34.28
	1.225	386	
	1.400	296	
	0.700	397	
	0.875	430	
22	1.050	392	31.87
	1.225	382	
	1.400	297	
	0.700	336	
	0.875	393	
23	1.050	383	34.93
	1.225	343	
	1.400	280	
	0.700	317	
	0.875	372	
24	1.050	361	36.35
	1.225	359	
	1.400	255	

Table A.2. (cont.) Planar device values for $f_i(x)$ and Channel Performance Ratio (CPR)

Channel, *i*	*x* (cm)	$f_i(x)$ (counts)	CPR
	0.700	386	
	0.875	391	
25	1.050	392	33.81
	1.225	349	
	1.400	265	
	0.700	605	
	0.875	643	
26	1.050	606	21.55
	1.225	539	
	1.400	386	
	0.700	589	
	0.875	600	
27	1.050	529	22.94
	1.225	527	
	1.400	362	
	0.700	374	
	0.875	370	
28	1.050	354	36.36
	1.225	332	
	1.400	202	
	0.700	385	
	0.875	376	
29	1.050	389	35.33
	1.225	321	
	1.400	184	

Table A.2. (cont.) Planar device values for $f_i(x)$ and Channel Performance Ratio (CPR)

Channel, *i*	*x* (cm)	$f_i(x)$ (counts)	CPR
	0.700	406	
	0.875	383	
30	1.050	397	34.13
	1.225	336	
	1.400	206	
	0.700	650	
	0.875	668	
31	1.050	649	20.52
	1.225	572	
	1.400	336	

Table A.3. 100-µm trenched device values for $f_i(x)$ and Channel Performance Ratio (CPR)

Channel, *i*	*x* (cm)	$f_i(x)$ (counts)	CPR
	0.700	4,002	
	0.875	5,163	
0	1.050	5,579	22.41
	1.225	5,809	
	1.400	5,537	
	0.700	1,780	
	0.875	2,381	
1	1.050	2,480	50.15
	1.225	2,632	
	1.400	2,396	
	0.700	8,288	
	0.875	9,988	
2	1.050	10,757	11.92
	1.225	10,676	
	1.400	9,763	
	0.700	3,523	
	0.875	3,896	
3	1.050	4,115	30.92
	1.225	4,060	
	1.400	3,567	
	0.700	1,152	
	0.875	1,416	
4	1.050	1,529	83.60
	1.225	1,537	
	1.400	1,408	

Table A.3. (cont.) 100-µm trenched device values for $f_i(x)$ and Channel Performance Ratio (CPR)

Channel, *i*	*x* (cm)	$f_i(x)$ (counts)	CPR
	0.700	989	
	0.875	1,229	
5	1.050	1,323	94.56
	1.225	1,382	
	1.400	1,282	
	0.700	1,147	
	0.875	1,596	
6	1.050	1,605	79.11
	1.225	1,652	
	1.400	1,419	
	0.700	894	
	0.875	1,149	
7	1.050	1,246	107.11
	1.225	1,145	
	1.400	1,064	
	0.700	3,005	
	0.875	3,578	
8	1.050	3,810	34.43
	1.225	3,624	
	1.400	3,161	
	0.700	1,596	
	0.875	1,900	
9	1.050	1,951	64.82
	1.225	1,915	
	1.400	1,765	

Table A.3. (cont.) 100-µm trenched device values for $f_i(x)$ and Channel Performance Ratio (CPR)

Channel, *i*	*x* (cm)	$f_i(x)$ (counts)	CPR
	0.700	3,654	
	0.875	4,296	
10	1.050	4,536	28.36
	1.225	4,330	
	1.400	4,042	
	0.700	6,255	
	0.875	7,095	
11	1.050	7,602	16.84
	1.225	7,603	
	1.400	6,579	
	0.700	3,236	
	0.875	4,014	
12	1.050	4,053	31.79
	1.225	3,994	
	1.400	3,292	
	0.700	3,355	
	0.875	3,867	
13	1.050	4,014	32.10
	1.225	3,862	
	1.400	3,356	
	0.700	7,428	
	0.875	8,000	
14	1.050	8,326	15.39
	1.225	7,989	
	1.400	6,785	

Table A.3. (cont.) 100-µm trenched device values for $f_i(x)$ and Channel Performance Ratio (CPR)

Channel, *i*	*x* (cm)	$f_i(x)$ (counts)	CPR
	0.700	1,237	
	0.875	1,247	
15	1.050	1,351	94.67
	1.225	1,302	
	1.400	1,124	
	0.700	2,207	
	0.875	2,596	
16	1.050	2,551	49.05
	1.225	2,549	
	1.400	2,172	
	0.700	2,841	
	0.875	2,969	
17	1.050	3,220	41.08
	1.225	2,948	
	1.400	2,427	
	0.700	3,214	
	0.875	3,555	
18	1.050	3,585	35.79
	1.225	3,439	
	1.400	2,738	
	0.700	1,102	
	0.875	1,263	
19	1.050	1,265	101.60
	1.225	1,169	
	1.400	1,032	

Table A.3. (cont.) 100-µm trenched device values for $f_i(x)$ and Channel Performance Ratio (CPR)

Channel, *i*	*x* (cm)	$f_i(x)$ (counts)	CPR
	0.700	3,378	
	0.875	3,831	
20	1.050	3,776	34.24
	1.225	3,471	
	1.400	2,794	
	0.700	3,137	
	0.875	3,313	
21	1.050	3,332	38.24
	1.225	3,214	
	1.400	2,451	
	0.700	4,852	
	0.875	5,477	
22	1.050	5,387	24.07
	1.225	4,917	
	1.400	3,875	
	0.700	2,541	
	0.875	2,790	
23	1.050	2,782	46.57
	1.225	2,582	
	1.400	1,968	
	0.700	2,576	
	0.875	2,851	
24	1.050	2,850	45.95
	1.225	2,564	
	1.400	1,981	

Table A.3. (cont.) 100-µm trenched device values for $f_i(x)$ and Channel Performance Ratio (CPR)

Channel, *i*	*x* (cm)	$f_i(x)$ (counts)	CPR
	0.700	2,227	
	0.875	2,281	
25	1.050	2,343	54.84
	1.225	2,175	
	1.400	1,751	
	0.700	10,424	
	0.875	11,242	
26	1.050	11,073	11.83
	1.225	9,826	
	1.400	6,850	
	0.700	4,141	
	0.875	4,531	
27	1.050	4,441	29.68
	1.225	3,782	
	1.400	2,799	
	0.700	2,799	
	0.875	3,099	
28	1.050	2,898	44.24
	1.225	2,606	
	1.400	1,751	
	0.700	2,531	
	0.875	2,597	
29	1.050	2,467	51.31
	1.225	2,232	
	1.400	1,502	

Table A.3. (cont.) 100-µm trenched device values for $f_i(x)$ and Channel Performance Ratio (CPR)

Channel, *i*	*x* (cm)	$f_i(x)$ (counts)	CPR
	0.700	5,180	
	0.875	5,605	
30	1.050	5,342	24.32
	1.225	4,663	
	1.400	3,011	
	0.700	7,851	
	0.875	8,093	
31	1.050	7,506	16.35
	1.225	7,438	
	1.400	4,725	